

Multi-reference protocol for (auto)ionization spectra: application to molecules

Gilbert Grell^{a)} and Sergey I. Bokarev

Institut für Physik, Universität Rostock, Albert-Einstein-Str. 23-24, 18059 Rostock, Germany

(Dated: December 10, 2019)

We present the application of the spherically averaged continuum model to the evaluation of molecular photoelectron and resonant Auger electron spectra. In this model, the continuum wave function is obtained in a numerically efficient way by solving the radial Schrödinger equation with a spherically averaged molecular potential. Different approximations to the Auger transition matrix element and, in particular, the one-center approximation are thoroughly tested against experimental data for the CH₄, O₂, NO₂, and pyrimidine molecules. In general, this approach appears to estimate the shape of the photoelectron and autoionization spectra as well as the total Auger decay rates with reasonable accuracy, allowing for the interpretation of experimental results.

I. INTRODUCTION

Photoionization and (resonant) autoionization processes encode the system's electronic structure into the kinetic energy of the ejected electrons, producing a Photoelectron Spectrum (PES) or a Resonant Auger Electron Spectrum (RAES), respectively. A particular advantage of these electron-out spectroscopies is that they map bound to continuum states and thus are not subject to selection rule suppression and are more flexible than optical spectroscopy.¹⁻³ For instance, the combination of X-ray valence PES and RAES has been used to unravel specific solute-solvent interactions of transition metal complexes in solutions.⁴⁻⁶ In addition, these processes can probe, initiate, and couple to complex electronic and nuclear dynamics.⁷⁻¹¹ Moreover, they can cause biological radiation damage by a cascade of autoionization events.^{12,13}

Often the resulting spectra are feature-rich and difficult to interpret based on the experimental data alone.^{6,14} Hence, the development of theoretical methods for the simulation of PES and RAES has accompanied the experimental advancement during the last decades. Notably, modelling ionization processes remains challenging until today, although the fundamental theory is been known for decades.¹⁵⁻¹⁸

Here, the most general framework is the multi-channel scattering formalism,¹⁷ treating continuum and bound states on the same level and including correlation effects between them.^{19,20} At this level of accuracy, solving the bound and continuum problems in a B-spline basis,²¹ specialized Gaussian basis sets,^{22,23} or combination of both²⁴ has proven to be a versatile approach for atoms, diatomics, and first-row hydrides.^{23,25-27}

More approximate approaches are usually obtained in the single-channel scattering formalism.²⁰ For example, the multi-centered B-spline static-exchange Density Functional Theory (DFT) method^{28,29} has been applied

to molecules reaching the size of small organometallic complexes.²⁹⁻³² Further, methods that project the molecular problem on a one-center expansion allow to evaluate PES and RAES of small molecular systems with remarkable accuracy.³³⁻³⁵ A particular efficient scheme is obtained, if the molecular continuum orbital problem is approximated by an atomic one.³⁶⁻⁴¹ Here, the simplest approach is to model the outgoing electron as a free particle or a distorted wave corresponding to an effective Coulomb potential,⁴²⁻⁴⁴ which has been in particular applied to PES studies of rather large molecules.⁴⁵⁻⁴⁹ Finally, an entirely different set of methods relies on an implicit continuum representation with Stieltjes imaging⁵⁰⁻⁵³ or a Green's operator formalism.⁵⁴ However, energies of several hundreds of eV, targeted in X-ray PES and RAES necessitate large basis sets leading to demanding computations.

In all these methods, there is a certain trade-off between the accuracy that can be afforded for modelling the bound states and the continuum part on the one side and the size of the system on the other. On the one pole, the multi-channel methods are residing which are highly accurate but computationally expensive and, thus, allow for treatment of only small systems. The other extreme is to neglect the multi-center molecular potential and use simplistic representations like the free-particle approach, sacrificing the accuracy in favor of computational feasibility. Moreover, most of the methods described above have a single reference character and are not suited to treat systems possessing multi-configurational wave functions, e.g., open-shell and transition metal compounds or dynamics near conical intersections.

In this article, we employ a multi-reference Quantum Chemistry (QC) protocol and present the Spherical Continuum for Ionization (SCI) approach for the evaluation of photoionization cross sections and partial Auger decay rates for the case of molecules. The central approximation in the protocol is that the angular structure of the molecular potential is averaged out, leading to spherically symmetric continuum orbitals that are obtained by numerically solving the radial Schrödinger equation.

^{a)} gilbert.grell@uni-rostock.de

Thus, it represents a compromise between the two extreme cases mentioned above. This work is a logical continuation of our previous benchmark of the protocol for the atomic case of RAES of the neon $1s^{-1}3p$ resonance, where it was shown to yield spectra and total decay rates in good agreement with experimental references.⁵⁵ Such an approach, being natural for atoms, requires a numerical justification for the non-spherically symmetric molecular case. As is demonstrated here, the SCI method indeed provides a valuable insight into the character of photoionization and autoionization molecular spectral features. In addition, we investigate the performance of the popular One-Center Approximation (1CA) to Auger decay,^{36,39,40,56} neglecting contributions from atoms other than the core-hole bearing one.

Concerning the applicability of the SCI ansatz, the crucial role is expected to be played by the deviations of the molecular point symmetry from the spherical one. In this respect, highly symmetric molecules should in general be more suitable objects for SCI representation, whereas for highly non-spherical systems, e.g., linear or planar, SCI model might represent a quite crude approximation. Therefore, we start the discussion with the K-edge spectra of CH_4 , being isoelectronic to neon studied previously,⁵⁵ which is the simplest system out of the selected series as it contains only one heavy atom and possesses a high symmetry. Increasing the complexity, we continue with the open shell molecules O_2 and NO_2 , allowing for ionization channels corresponding to different spins of ionic remainder, and address the K-edges of oxygen and nitrogen, respectively. The largest object studied herein is the pyrimidine ($\text{C}_4\text{H}_4\text{N}_2$) which is an aromatic heterocyclic system, where we aim at description of nitrogen K-edge. For O_2 and pyrimidine, there is ambiguity in selecting the origin of the spherically symmetric continuum orbital because of presence of two equivalent atoms, which makes them also interesting objects for testing.

One should note that for such small molecules vibrational effects, showing up as, e.g. vibronic progressions in the (auto)ionization spectra, are of importance and alter the measured experimental spectrum.⁵⁶ Furthermore, they can lead to emergence of a measurable signal, even if a purely electronic transition is forbidden, due to vibronic interactions⁵⁷ or show up in new features appearing due to the ultrafast dissociation.⁵⁸ In this work, we considered only electronic effects since the main goal is to test our multi-reference protocol for the case of molecules. The full treatment, however, would require the inclusion of the nuclear motion into the consideration.

The article is organized as follows. First, we briefly recapitulate the theory behind our approach in Section II, which is presented in detail elsewhere,⁵⁵ and give the details of our computational setup in Section III. The X-ray Absorption Spectrum (XAS), RAES, and valence PES are discussed on a case to case basis for each molecule separately in Section IV. The overall summary across the series of molecules under study is given in Conclusions, Section V.

II. THEORY

In this section, we briefly present theory behind our method; the detailed description can be found in our recent article.⁵⁵ Atomic units (a.u.) are employed throughout this article, if not stated otherwise. We restrict ourselves to the limits of first order perturbation theory, dipole approximation, and length gauge for the absorption and photoionization cross sections σ_{gi} and $\sigma_{g\alpha}$. Further, the average over the molecular orientation with respect to the polarization vector of the incoming light is taken. Finally, the nonradiative decay rates $\Gamma_{i\alpha}$ are estimated within the two-step model,⁵⁹ neglecting the excitation process and the interference of decay and direct ionization pathways. The resulting expressions for XAS, PES, and RAES read

$$\sigma_{gi} = \frac{4\pi^2}{3c} \omega |\langle \Psi_i | \boldsymbol{\mu} | \Psi_g \rangle|^2, \quad (1)$$

$$\sigma_{g\alpha} = \frac{4\pi^2}{3c} \omega k |\langle \Psi_\alpha | \boldsymbol{\mu} | \Psi_g \rangle|^2, \quad (2)$$

$$\Gamma_{i\alpha} = 2\pi |\langle \Psi_\alpha | \mathcal{H} - \mathcal{E}_i | \Psi_i \rangle|^2, \quad (3)$$

respectively.^{16,19,60} Here, $|\Psi_g\rangle$ denote the ground state, $|\Psi_i\rangle$ are intermediate core-excited states (resonances), and $|\Psi_\alpha\rangle$ are ionized continuum states (autoionization channels) of the system. Further, $\boldsymbol{\mu} = -\sum_{u=1}^N \mathbf{r}_u$ is the N -electron dipole operator, $\mathcal{H} = \sum_u h_u + \sum_{u<v} 1/r_{uv}$ is the molecular Hamiltonian, containing one-electron h_u and two-electron $1/r_{uv}$ parts respectively, and \mathcal{E}_i , ω , and k are the energies of $|\Psi_i\rangle$, of the incoming radiation as well as the wavenumber of the ionized electron, respectively. To ensure that the total spin and its projection onto the quantization axis for the unionized system, S and M , are conserved, the continuum states are constructed as

$$|\Psi_\alpha\rangle = \sum_{M^+ = -S^+}^{S^+} \sum_{\sigma = -\frac{1}{2}, \frac{1}{2}} C_{S^+, M^+; \sigma}^{S, M} |\Upsilon_\alpha^{\sigma M^+}\rangle, \quad (4)$$

where $|\Upsilon_\alpha^{\sigma M^+}\rangle = a_{\alpha, \sigma}^\dagger |\Psi_{f, M^+}^+\rangle$ are channel functions corresponding to the bound cationic states $|\Psi_{f, M^+}^+\rangle$ with an additional electron, created by $a_{\alpha, \sigma}^\dagger$, in the continuum orbital $|\psi_{\alpha, \sigma}\rangle$. The $C_{S^+, M^+; \sigma}^{S, M}$ are the Clebsch-Gordan coefficients; note that S^+ and M^+ correspond to the total spin and its quantization axis projection of the ionic remainder.

The central approximation of the SCI approach is to employ the spherically averaged molecular potential of the ion and thus spherically symmetric continuum orbitals

$$\psi_{\alpha, \sigma}(r, \Omega) = \frac{1}{r} w_l^{fk}(r) Y_l^m(\Omega) \zeta(\sigma), \quad (5)$$

where spherical harmonics $Y_l^m(\Omega)$, $\zeta(\sigma)$, and $w_l^{fk}(r)$ correspond to the angular, spin, and radial parts of the

wave function, respectively. The compound channel index $\alpha = (f, l, m, k)$ contains the index of the ionic bound state f , the angular and magnetic quantum numbers l and m , and the wave number $k = \sqrt{2\varepsilon_\alpha}$ of the outgoing electron. For the evaluation of the spectra, one needs to sum over all decay channels α and in particular l and m . The energy of the outgoing electron is

$$\varepsilon_\alpha = \begin{cases} \omega + \mathcal{E}_g - \mathcal{E}_f, & \text{direct ionization} \\ \mathcal{E}_i - \mathcal{E}_f, & \text{Auger decay} \end{cases} \quad (6)$$

In contrast to the atomic case,⁵⁵ for a molecule the origin of the continuum orbital, \mathbf{r}_c , and the molecular coordinate system in general differ. In fact, the location of \mathbf{r}_c is often ambiguous. Thus $\mathbf{r}_s = \mathbf{r} - \mathbf{r}_c$ defines the reference frame for Eq. (5). The functions $w_l^{fk}(r)$ are numerical solutions to the radial Schrödinger equation with the spherically averaged direct Coulomb potential $V_f^J(r) = V^{\text{nuc}}(r) + J_f(r)$ of the cationic state $|\Psi_{f,M^+}^+\rangle$ defined in spherical coordinates $\mathbf{r}_s = (r, \Omega)$ and containing nuclear $V^{\text{nuc}}(r)$ and electronic $J_f(r)$ parts. They are computed using Numerov's method on a radial grid. Asymptotically the solutions are constructed such as to fulfill the conditions

$$w_l^{fk}(r \rightarrow 0) = nr^{l+1}, \quad (7a)$$

$$w_l^{fk}(r \rightarrow \infty) = \sqrt{\frac{2}{\pi k}} \left(\cos \delta_l^f(k) F_l(\eta, kr) + \sin \delta_l^f(k) G_l(\eta, kr) \right). \quad (7b)$$

Therein $\delta_l^f(k)$ are the scattering phases and F_l and G_l are the regular and irregular Coulomb functions,⁶¹ respectively.

The nuclear part of $V_f^J(r)$, corresponding to the nuclear charges being smeared out over a sphere around the photoelectron origin, resembles the classical potential of charged hollow spheres with the radii $R_{cA} = |\mathbf{r}_c - \mathbf{R}_A|$ and charge Z_A

$$V^{\text{nuc}}(r) = \sum_A \begin{cases} -\frac{Z_A}{R_{cA}}, & r < R_{cA} \\ -\frac{Z_A}{r}, & r \geq R_{cA} \end{cases}. \quad (8)$$

The electronic part $J_f(r)$, however, is the electrostatic potential of the spherically averaged electron density of the respective ionized state, which has to be determined numerically within the \mathbf{r}_s reference frame.⁵⁵

To keep this approach flexible with respect to the electronic structure method, we only require that the bound state wave functions are expressed as Configuration Interaction (CI) expansions built on the Molecular orbitals (MOs) expressed in terms of conventional Gaussian type orbital basis sets. Further, it is assumed that the neutral and cationic states have been obtained in separate calculations, comprising different relaxed sets of N_{orb} spin orbitals $\{\varphi_i\}$ and $\{\varphi_i^+\}$, respectively. Finally, the Strong Orthogonality (SO) approximation is employed throughout this work, since previous investigations⁵⁵ have shown

that quite reliable results can be obtained with it. Hence, the overlap between the continuum and bound orbitals is neglected.

For a particular ionization channel function this yields

$$\langle \Upsilon_\alpha^{\sigma M^+} | \boldsymbol{\mu} | \Psi_g \rangle \stackrel{\text{SO}}{=} - \langle \psi_{\alpha,\sigma} | \mathbf{r} | \Phi_{g\alpha}^{M^+} \rangle, \quad (9)$$

and the Auger decay matrix element reads

$$\begin{aligned} & \langle \Upsilon_\alpha^{\sigma M^+} | \mathcal{H} - \mathcal{E}_i | \Psi_i \rangle \\ & \stackrel{\text{SO}}{=} \langle \psi_{\alpha,\sigma} | h | \Phi_{i\alpha}^{M^+} \rangle + \underbrace{\sum_{q=1}^{N_{\text{orb}}} \langle \psi_{\alpha,\sigma} \varphi_q^+ | \frac{1}{r_{12}} | \Xi_{i\alpha}^{M^+,q} \rangle}_{r^{-1} \text{ coupling}}. \end{aligned} \quad (10)$$

Here, the matrix elements have been transformed to one and two-body integrals in terms of the corresponding Dyson orbitals $|\Phi_{n\alpha}^{M^+}\rangle$ ($n = i, g$) and two-electron reduced transition densities $|\Xi_{i\alpha}^{M^+,q}\rangle$. Formal details and the numerical procedure to evaluate the continuum-bound matrix elements are elucidated in Ref. 55. A popular approximation to the full Auger matrix element (\mathcal{H} coupling) is to disregard the one-electron terms, only accounting for the electronic Coulomb interaction (r^{-1} coupling). Further, the 1CA can be applied on top of the r^{-1} coupling to reduce the computational demands. Therein, the continuum orbital is placed on the core vacancy bearing atom and non-local contributions from all other atoms to the matrix element in Eq. 10 are neglected. The performance of the \mathcal{H} and r^{-1} couplings as well as of the 1CA has been investigated here.

III. COMPUTATIONAL DETAILS

For the molecules apart from oxygen, the geometries have been obtained with the GAUSSIAN09⁶⁶ program at the B3LYP/aug-cc-pVTZ level. For oxygen, we have employed the experimentally determined equilibrium distance of $r = 1.208 \text{ \AA}$.⁶⁷ The molecular symmetry has been restricted to the T_d (CH_4) and C_{2v} (NO_2 and pyrimidine) point groups.

For the joint discussion of the XAS, PES and RAES on equal footing, the underlying electronic structure calculation needs to satisfy all the demands for the involved electronic states. In fact, this requires accurate predictions of the ground and core-excited states of the neutral species, as well as of the cationic valence-excited states. For this purpose we have selected the Restricted Active Space Self-Consistent Field (RASSCF)/Restricted Active Space Second Order Perturbation Theory (RASPT2)^{68,69} approach. The active space is subdivided into the RAS1, RAS2, and RAS3 subspaces. The RAS1 contains o fully occupied orbitals, allowing for h holes at maximum. The occupation of the c orbitals within RAS2 is not restricted, corresponding to a full CI treatment within this subspace.

Table I. QC schemes used for the bound electronic structure calculations of the depicted molecules: employed basis set, active space, imaginary shift used in the respective PT2 calculation, and number of electronic states per charge/multiplicity of the molecule. The number of electrons in the active space corresponds to the neutral species. ANO-L⁶² basis functions have been used in all cases.

	Basis Set	Active Space	δ_{PT2} [a.u.]	Nr. of States	Comment
CH ₄	C: [7s5p3d2f] ^a	RAS(10, 1, 1; 1, 4, 19)	0.01	¹ CH ₄ : 96 ² CH ₄ ⁺ : 308	SupSym ^c
	H: [3s2p1d]	RAS1: 1a ₁ , RAS2: 2a ₁ , 1t ₂ RAS3: 3s(a ₁), 3p(t ₂), 3d(t ₂), 3d(e), 4s(a ₁), 4p(t ₂), 4d(t ₂), 4d(e), 5s(a ₁)			
O ₂	[5s4p2d1f]	RAS(16, 2, 0; 2, 8, 0)	0.1	³ O ₂ : 826 ² O ₂ ⁺ : 1008 ⁴ O ₂ ⁺ : 504	Linear ^c
		RAS1: 1σ _u , 1σ _g			
		RAS2: 2-3σ _g , 2-3σ _u , 1π _u , 1π _g			
NO ₂	N: [5s4p2d1f]	CAS(19; 11)	0.3	² NO ₂ : 430 ¹ NO ₂ ⁺ : 825 ³ NO ₂ ⁺ : 990	O(1s) frozen
	O: [5s4p2d1f]	CAS: 2-6a ₁ , 1a ₂ , 1-2b ₁ , 2-4b ₂			
C ₄ H ₄ N ₂	N: [4s3p2d1f]	RAS(34, 1, 1; 2, 15, 8)	0.2	¹ C ₄ H ₄ N ₂ : 137 ² C ₄ H ₄ N ₂ ⁺ : 2297	SupSym ^c C(1s) frozen
	C: [4s3p2d1f]	RAS1: σ(1a ₁), σ(1b ₂)			
	H: [3s2p1d]	RAS2: σ(5-10a ₁), σ(3-6b ₂), π ₁ (1b ₁), π ₂ (1a ₂), π ₃ (2b ₁), n _{N-} (7b ₂), n _{N+} (11a ₁)			
		RAS3: π*(2a ₂), π*(3-4b ₁), σ ^{Ryd} (12-13a ₁), π ^{Ryd} (5-6b ₁), π ^{Ryd} (3a ₂)			

^a ANO-L exponents⁶² have been supplemented by (8s6p6d4f) Rydberg exponents generated according to the procedure in Ref. 63. The (22s15p10d7f)/[7s5p3d2f] contractions have been obtained with the GENANO module⁶⁴ of OPENMOLCAS.⁶⁵, see Supplement: Section III.

^c Keyword used in the RASSCF calculation in MOLCAS 8.0 to prevent mixing of orbitals from different symmetries during the Self-Consistent Field (SCF) procedure.

RAS3, however, contains v virtual orbitals occupied by at most p electrons. Herein, we denote the total number of active electrons as a , which allows to uniquely specify each active space as RAS($a, h, p; o, c, v$). If only the RAS2 space is used, it corresponds to the Complete Active Space Self-Consistent Field (CASSCF)⁷⁰ calculation. In this case, the active space is denoted as CAS($a; c$). Due to the restricted configuration space central to these methods, the wave functions are often lacking dynamic correlation effects. This is corrected to the second order of perturbation theory with the RASPT2⁶⁹ and CASPT2⁷¹ methods. All calculations have been conducted with a locally modified version of MOLCAS 8.0.⁷² The QC setups, i.e., the used basis sets, active spaces, number of states included in the state averaged SCF procedure, special keywords, and imaginary shifts within the PT2 correction are detailed for each system in Table I.

The Dyson orbitals and two-electron reduced transition densities in Eqs. (9) and (10) have been estimated using the biorthonormally transformed orbital and CI coefficients⁷³ for the neutral and cationic states.

IV. RESULTS AND DISCUSSION

We have chosen to present all ionization spectra with respect to the electronic binding energies rather than the kinetic energies. This introduces a common reference for PES and RAES irrespective of the photon energy at

which they have been obtained, simplifying the analysis. To allow for a uniform comparison, both the simulated results and the digitized experimental spectra have been aligned with respect to the lowest vertical Ionization Potentials (IPs) of each molecule, taken from Refs. 74–77. In case of methane, the 2a₁⁻¹ IP has been used because the respective bands are narrower than the lowest 1t₂⁻¹ ones. Note that for the open shell systems O₂ and NO₂ each ionization branch differing in the spin of the final ion was shifted individually in our simulated spectra. The calculated XAS have been shifted as well. All applied shifts are summarized in Table II. The broadening parameters for the XAS, PES, and RAES of all molecules, tuned for the best agreement between our theory and the reference, are detailed in Supplement: Section II.

A. Methane

CH₄ has been chosen because it is isoelectronic to the previously investigated neon atom⁵⁵ and thorough studies regarding its XAS, PES and RAES have been carried out both experimentally^{57,78,79} and theoretically.^{80,81} In addition, its tetrahedral symmetry with the central carbon atom closely resembles spherical symmetry, indicating that the SCI approach could be well suited to study ionization processes in this case. In Fig. 1, we compare our theoretical results for the XAS, PES, and RAES from various resonances to experimental reference data

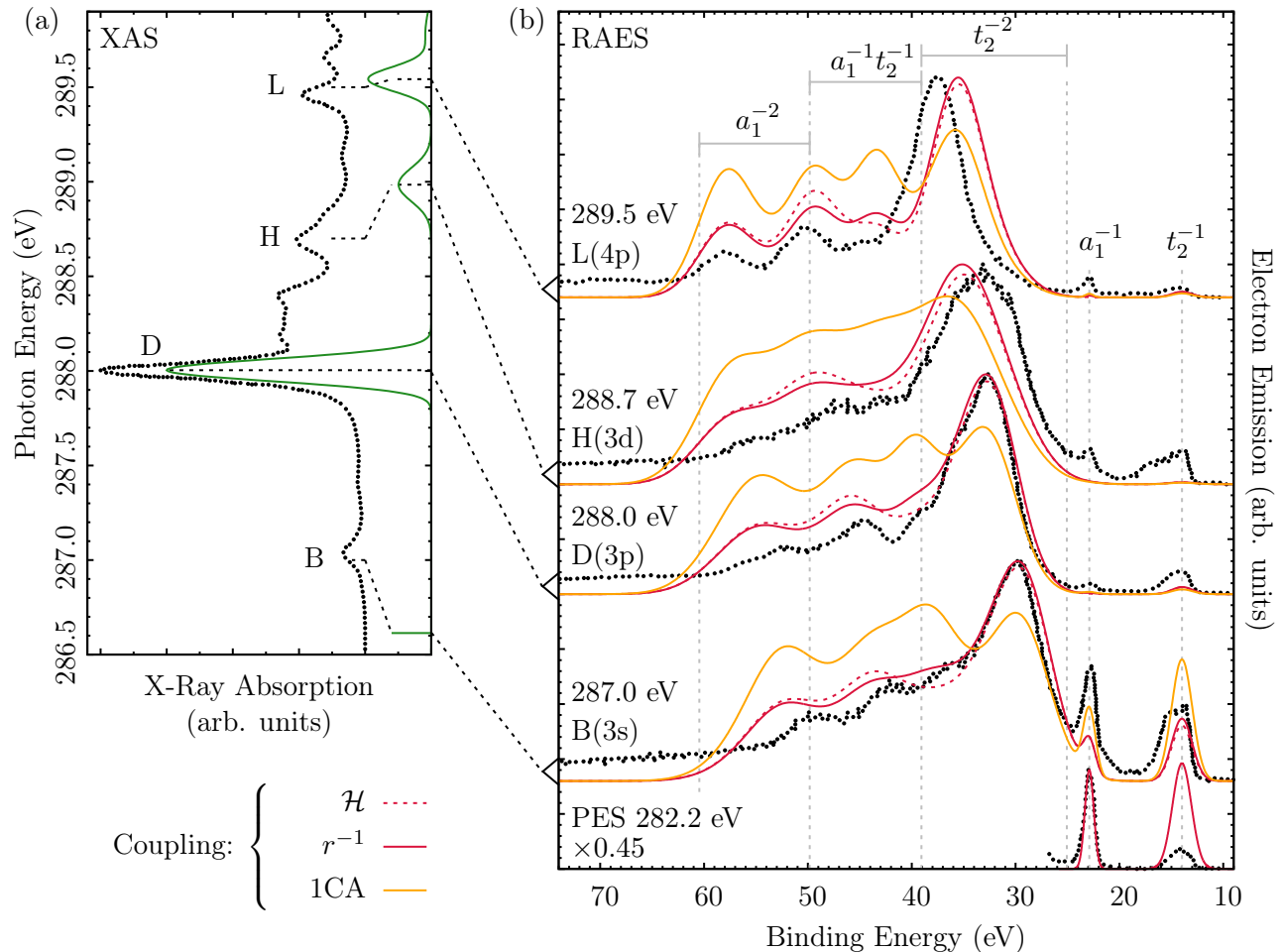


Figure 1. (a) Calculated XAS of methane at the carbon K-edge (green, solid) compared to the experimental result (black, dotted). The position of the dipole-forbidden excitation to the $3s(a_1)$ orbital at 286.6 eV is indicated by a single stick. The assignment of the experimental data follows Refs. 78 and 79 and has been connected to the corresponding core-excited states in our calculation (dashed). (b) RAES obtained with our method using the SCI model together with the respective measured spectra. The key for the coupling types is given under panel (a). All simulated spectra for one resonance have been normalized with the same constants to underline their differences. Dominant Rydberg contributions obtained in our calculation (in paranthesis) as well as the excitation energies used in the experiment are given for guidance. The experimental and theoretical valence PES taken at a photon energy of 282.2 eV are shown at the bottom as well. Note that all experimental data in this figure have been digitized from Kivimaeki et al.⁵⁷ Shifts and broadening parameters are detailed in Table II and the main text.

digitized from Kivimäki et al.⁵⁷ Therein, the ionization spectra have been recorded using a magic angle geometry,⁸² eliminating angular anisotropy effects that have not been covered in our angle-integrated spectra.

a. XAS Fig. 1(a) contains the experimental⁵⁷ and calculated XAS. Both spectra are normalized to the D($3p$) peak and the experimental data are shifted by 2 units of intensity for clarity. Below we use the notation of bands from Ref. 57. Note that we always omit the core orbital from the labeling of resonances here and in the following, unless explicitly required.

The experimental spectrum comprises a wealth of features. The assignment of them is complicated by the strong vibronic coupling especially for higher transition energies,^{78,79} which is not included in our consideration.

For instance, the B($3s$) peak is due to the dipole forbidden $3s(a_1)$ core excitation which becomes allowed due to a coupling to t_2 vibrational modes with a frequency of 0.374 eV.⁷⁹ This fits well to the offset of -0.4 eV in the resonance position predicted in our calculation. The remaining peaks have been assigned as follows. D($3p$) corresponds to the $3p(t_2)$ resonance and according to the literature^{78,79} should be free of vibrational effects. H($3d$) is a $3d(t_2)$ resonance in accordance with Ref. 78 and is shifted by 0.3 eV with respect to the experiment. However, it may also be ascribed to a mixed $3d(t_2)$ /vibrationally excited $3p(t_2)$ character which might explain the obtained shift.⁵⁷ Finally, L($4p$) calculated with a slight offset of 0.1 eV is assigned to the $4p(t_2)$

Table II. The respective reference IPs and shifts (in eV) for the alignment of the theoretical and experimental ionization and absorption spectra. The experimental shifts have been applied to the indicated properties (see respective footnotes), whereas the theoretical ones have been uniformly applied to all PES and RAES for each system.

	vertical IP ^a	$\Delta_{\text{Theory}}^{\text{Ion}}$	$\Delta_{\text{Exp}}^{\text{Ion}}$	$\Delta_{\text{Theory}}^{\text{XAS}}$
CH ₄	22.90 ⁷⁴ ($2a_1^{-1}$)	-0.670	0.110 ^b	-0.850
			-0.260 ^c (B)	
			-0.300 ^c (D)	
			0.200 ^c (H)	
			0.060 ^c (L)	
O ₂	12.33 ⁷⁵ (${}^2O_2^+$)	-0.120	-0.100 ^b	0.294
			16.70 ⁷⁵ (${}^4O_2^+$)	
NO ₂	11.25 ⁷⁶ (${}^1NO_2^+$)	-0.056	0.125 ^b	-0.938
			13.02 ⁷⁶ (${}^3NO_2^+$)	
C ₄ H ₄ N ₂	9.81 ⁷⁷	0.200	-	2.680

^a The final state of the ion is given in parentheses.

^b PES

^c RAES

resonance.^{78,79} However, because of the aforementioned strong vibronic coupling other electronic states might contribute to this peak as well.⁷⁹ Generally, taking into account the absence of vibrational effects in our calculations, the relative energetic positions of the Rydberg resonances and their XAS intensities are in good agreement with the experiments.

b. PES and RAES Panel (b) of Fig. 1 shows the theoretical and experimental⁵⁷ RAES taken at the indicated resonance energies. Further, the valence PES, recorded at 282.20 eV are depicted. Complete, \mathcal{H} , and approximate, r^{-1} , couplings as well as the 1CA of the r^{-1} coupling were employed to evaluate the partial decay rates. To ensure convergence of the spectral intensities with respect to the continuum orbital angular momentum l , we took into account partial waves up to $l_{\text{max}} = 5$ (1CA RAES) and $l_{\text{max}} = 12$ (PES, \mathcal{H} , and r^{-1} RAES). This is natural, since the 1CA results correspond to matrix elements centered at one atom and thus converge faster in l .

Finally, the PES and RAES have been normalized to the a_1^{-1} and t_2^{-2} features, respectively. Note that the normalization constants determined for the r^{-1} RAES have been used for the 1CA and \mathcal{H} spectra as well to underline their relative differences.

The valence PES contains two peaks corresponding to electron emission from the $2a_1$ and $1t_2$ valence orbitals, leading to single hole states depicted as a_1^{-1} and t_2^{-1} . Apparently, our model can not reproduce the relative PES intensities of these peaks correctly at this excitation energy and overestimates the intensity of the t_2^{-1} feature by a factor of 4. A study of the PES with different model potentials (Supplement: Fig. S1) has revealed that the spectrum depicted in Fig. 1, employing $V_f^J(r)$, yields in fact the best agreement possible within our present model. A

further improvement would require a non-spherical continuum model that accounts for the true molecular symmetry. However, the $a_1^{-1} : t_2^{-1}$ intensity ratio is quite sensitive to the photon energy,^{83,84} which suggests that this is a somewhat difficult case.

The RAES can roughly be divided into the participator and spectator decay regions, below and above 25 eV binding energy. Participator decay involves the excited electron in the decay process, leading to single hole states that are the main PES features as well. Here, the corresponding states are a_1^{-1} and t_2^{-1} , indicated by the dashed lines. Spectator decay, in contrast, leaves the excited electron intact and leads to states with two holes in the valence shell. Similar states result from normal Auger decay as well, albeit the additional electron introduces energetic shifts in the resonant case. The dominant character of the respective two hole states obtained in our calculation is indicated at the top of panel (b). Clearly the spectator decay is dominating the RAES. The main peak located in the range 25 – 40 eV is due to t_2^{-2} target states for all resonances. The high energy tail however generally comprises three features for all but the H resonance, where vibrational effects lead to a stronger broadening that hides the detailed structure in the experimental data. With decreasing binding energy, the first feature may be assigned to a_1^{-2} states, while the latter two can be assigned to states of $a_1^{-1}t_2^{-1}$ character. The participator region is most prominent for the B(3s) resonance.

Fig. 1 (b) demonstrates that the theoretical spectra obtained with \mathcal{H} and r^{-1} coupling reproduce the experimental RAES for all resonances with good accuracy. Note that using a simple effective Coulomb potential $-1/r$ to obtain the continuum orbitals leads to considerably worse agreement, see Supplement: Fig. S2. Further, employing an additional radial Slater exchange term into the potential does not improve the results, see Supplement: Fig. S3. With respect to the r^{-1} results, the \mathcal{H} coupling introduces just a slight redistribution of intensity from the high energy flank of the t_2^{-2} peak to the center of the high energy tail (about 45-50 eV). In contrast, employing the 1CA leads to an overestimation of the tail (>40 eV) and participator regions, whereas the main feature is underestimated. Thus, it seems that non-local contributions from the hydrogen atoms can not be disregarded and the 1CA is not a suitable approximation when evaluating RAES of methane with the SCI approach. In the remainder of this section, we will only refer to the results obtained with \mathcal{H} and r^{-1} coupling.

While the overall agreement for the \mathcal{H} and r^{-1} couplings is very good, the following differences remain. For all resonances, the a_1^{-2} and $a_1^{-1}t_2^{-1}$ regions are slightly overestimated with respect to the main t_2^{-2} feature. Further, the features in the tail region are blue shifted by roughly 3.0 eV and 2.0 eV for the B(3s) and D(3p) resonances, while for the H(3d) resonance the whole spectrum appears to be blue shifted by 1.0 eV. In contrast for L(4p), the t_2^{-2} feature appears red shifted by 2.0 eV,

which decreases towards higher binding energies to 0.5 eV for the a_1^{-2} peak. We attribute these shifts to the fact that our active space does not allow to include enough electron correlation to represent the highly excited states of CH_4^+ with the same accuracy as the lower ones. In addition, the lack of nuclear effects prohibits the description of shifts due to vibronic coupling in the resonances as well as the ionized states. Finally, the a_1^{-1} and t_2^{-1} participator peaks are barely present for the H(3d) and D(3p) resonances and the a_1^{-1} peak seems to be generally underestimated with respect to the t_2^{-1} one. This discrepancy is most probably due to the two-step approach to resonant Auger emission employed herein, disregarding the excitation process and the interference between photoionization and the Auger decay terms. Further, the deficiencies of our SCI model to describe the correct $a_1^{-1} : t_2^{-1}$ intensity ratio in the PES, might translate to the participator decay as well.

We conclude this discussion with the observation that the relative energetic positions and intensities of the features in the methane B(3s), D(3p), H(3d), and L(4p) RAES can be reproduced quite well with the SCI approach, using the $V_f^J(r)$ potential together with \mathcal{H} or r^{-1} coupling, while vibrational effects can be disregarded in a first approximation. The 1CA, however, is not enough to reproduce the relative intensities. Further, an improved model of the continuum orbital seems to be required to recover the $a_1^{-1} : t_2^{-1}$ intensity ratio in the PES at this energy.

B. Molecular oxygen

Being a biradical open shell system with triplet ground state multiplicity, molecular oxygen is an intriguing system, allowing for ionization into doublet and quartet spin states and being targeted by many studies. Especially the core-hole decay of O_2 has been subject to frequent investigation, since it is a textbook example of strong lifetime-vibrational interference effects.⁸⁶⁻⁸⁸ The plethora of available experimental data regarding its XAS^{85,89,90}, PES^{58,86} and RAES^{58,86,90,91} allows for a detailed test of our approach.

The homonuclear linear geometry of O_2 suits to test the applicability of the spherically symmetric continuum orbital model that is central to our protocol. For instance, the 1s core hole might be delocalized over both atoms, whereas we expect our method to be more appropriate in the case of a localized hole. Further, it introduces some ambiguity regarding the coordinate origin of the continuum wave functions, see Section II, which might be placed either on one atom, \mathbf{R}_O , or at the interatomic center $\bar{\mathbf{R}}_{\text{O}_2}$. Both approaches have been tested here with respect to their ability to reproduce the PES and RAES of O_2 .

a. XAS The comparison of the theoretical K-edge XAS of O_2 against experimental data that has been digitized from Ma et al.⁸⁵ is presented in Fig. 2 (a).

Both spectra were normalized to the dominating peak at 531 eV that corresponds to core excitations to the $1\pi_g$ orbitals.⁸⁵ The structured double peak at 539-545 eV has been assigned to two broad $3\sigma_u$ resonances that are exchange split by 2.3 eV and a series of Rydberg excitations.⁸⁵ We recover this characteristic in our theory, however the splitting is smaller being about 1.4 eV, which can be attributed to the missing Rydberg orbitals in our active space. In agreement with Ref. 85, we find the following assignment. The lower energy feature at 539.3 eV predominantly corresponds to the promotion of a spin-up (α) electron to the $3\sigma_u$ orbital, i.e., quartet spin coupling in the valence shell, which we denote as $q\text{-}3\sigma_u$ in the following. The higher energy peak at 540.7 eV comprises doublet spin coupling in the valence shell, labeled analogously as $d\text{-}3\sigma_u$. Further, a small feature at 535.5 eV is not found in the experimental data, while the one at 547.5 eV is already above the core ionization threshold.⁹² The former corresponds to the shake-up excitation of 1.0 core and 0.6 valence electrons to the $1\pi_g$ orbitals, while the latter is due to states involving simultaneous excitations to the $1\pi_g$ and $3\sigma_u$ orbitals.

The photon energy of 530.8 eV at which Caldwell et al.⁵⁸ have recorded the RAES has been assigned to the $1\pi_g$ resonance. However, due to the bandwidth of ~ 2.7 eV in the experimental setup, the excitation at 540.0 eV involves both exchange-split $q\text{-}3\sigma_u$ and $d\text{-}3\sigma_u$ resonances. Notably, the evaluated core holes are $1\sigma_g^{-0.3}1\sigma_u^{-0.7}$ and $1\sigma_g^{-0.65}1\sigma_u^{-0.35}$ for the $1\pi_g$ and both $3\sigma_u$ resonances, respectively, i.e., they are delocalized in our calculation.

b. PES and RAES In Fig. 2(b), the computed PES and $1\pi_g$ as well as $q\text{-}3\sigma_u$ and $d\text{-}3\sigma_u$ RAES of O_2 are compared to the experimental data recorded under the pseudo magic angle of 57° by Caldwell et al.⁵⁸ The respective spectra have been normalized to the heights of the features P1, R4, and S3. The continuum orbitals have been generated with the $V_f^J(r)$ potential, centered either at \mathbf{R}_O or $\bar{\mathbf{R}}_{\text{O}_2}$. Further, the partial decay rates have been estimated using the complete, \mathcal{H} , and approximate, r^{-1} , couplings. Results obtained with the 1CA for the \mathbf{R}_O origin are shown as well. Note the remarkably different convergence of the results with respect to highest angular momentum included in the photoelectron representation: it was necessary to include waves up to $l_{\text{max}} = 12$ for the PES, $l_{\text{max}} = 15$ for the RAES with \mathcal{H} and r^{-1} couplings, and $l_{\text{max}} = 5$ in case of 1CA RAES.

The experimental RAES and PES are quite structured and feature-rich. Remarkably, the energetic positions of experimental PES features are reproduced almost exactly. Using the SCI approach we have been able to achieve quite good overall agreement with the experimental $1\pi_g$ RAES. Reproducing the $3\sigma_u$ spectrum is more problematic, because the $q\text{-}3\sigma_u$, $d\text{-}3\sigma_u$ and underlying Rydberg resonances,⁸⁵ which are not included here, are simultaneously excited in the experiment.

In the PES, P1 and P3 correspond to the $2^1\pi_g^{-1}$ and $2^3\sigma_g^{-1}$ ionic final states, respectively. P2, hav-

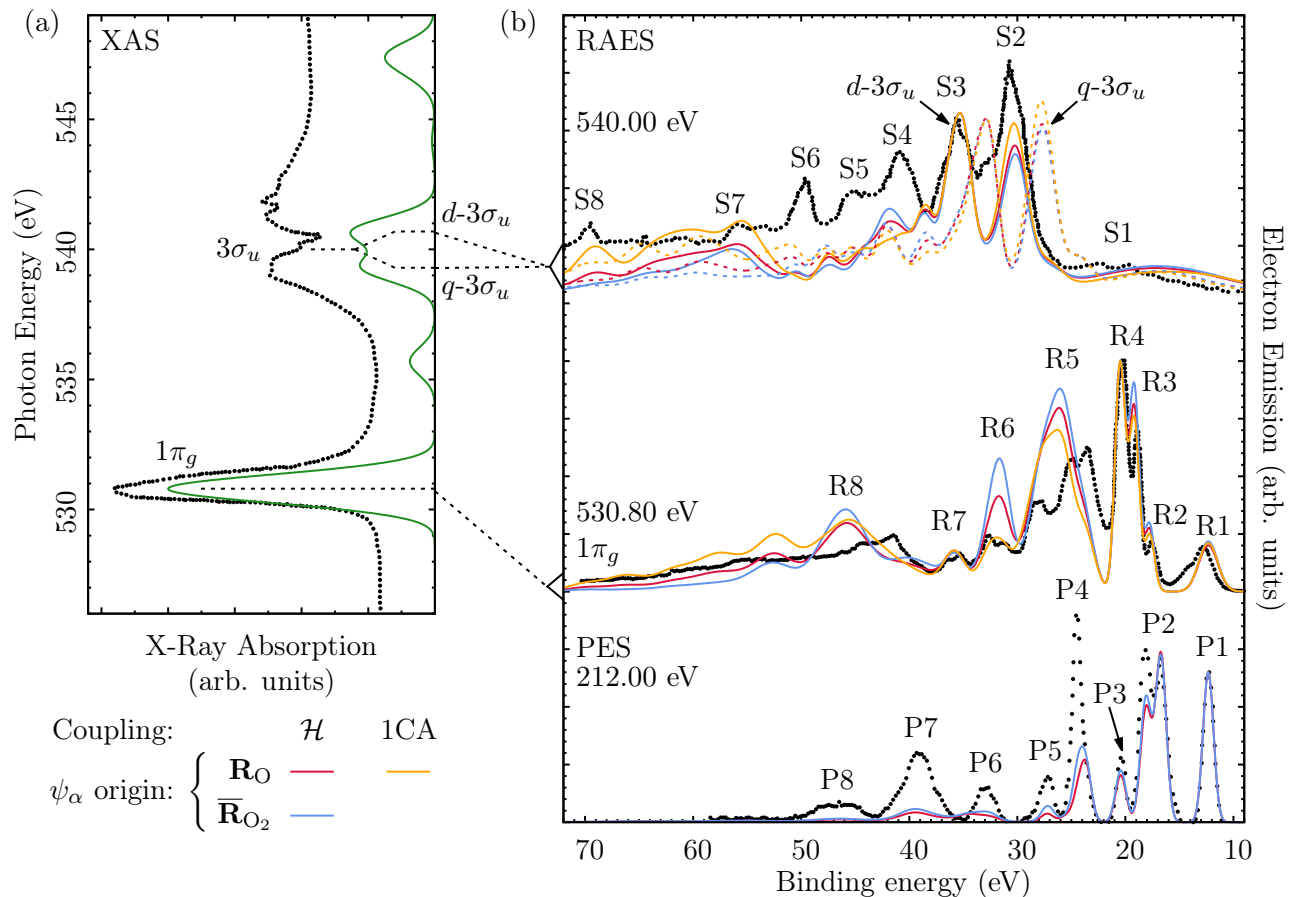


Figure 2. (a) Calculated K-edge XAS of O_2 (solid) compared against experimental results from Ma et al.⁸⁵ (dotted). The experimental excitation energies are connected to the theoretically found $1\pi_g$, $q-3\sigma_u$, and $d-3\sigma_u$ resonances in the XAS, as well as to the respective RAES in (b). Therein, the theoretical RAES and PES obtained with the SCI approach are presented together with the respective experimental data that has been digitized from Caldwell et al.⁵⁸ (dotted). Note that due to the high bandwidth of ~ 2.5 eV, the whole exchange split $3\sigma_u$ double peak is excited by the incoming radiation at 540 eV. Hence, the theoretical RAES for the $q-3\sigma_u$ (dashed) and $d-3\sigma_u$ (solid) resonances are depicted in this case. The theoretical results have been obtained with continuum orbitals corresponding to the $V_f^J(r)$ potential originating either at one atom, \mathbf{R}_O , or at the molecular center, $\overline{\mathbf{R}}_{O_2}$, as well as with the indicated coupling approaches. All spectra have been normalized. The applied shifts and broadenings are detailed in Table II and Supplement: Table S2, respectively.

ing a double peak structure, is due to primarily quartet cationic states: $^41\pi_u^{-1}$ at 17 eV and $^43\sigma_g^{-1}$ with a smaller contribution from $^2\pi_u^{-1}$ at 18 eV, respectively. P4 contains already combination transitions with the leading states $^21\pi_u^{-1}$ and $^42\sigma_u^{-0.5}3\sigma_g^{-0.5}$ which are accompanied by excitations to the σ and π orbitals. P5 corresponds to the double hole states $^43\sigma_g^{-1}1\pi_u^{-0.75}1\pi_g^1$ and $^22\sigma_u^{-0.3}3\sigma_g^{-0.6}1\pi_u^{-0.5}1\pi_g^{0.5}$. The higher binding energy features increasingly correspond to states carrying multiple excitations that can hardly be assigned in the orbital picture. Note that our analysis is in accord with that of Ref. 75.

The calculated PES intensities quite well reproduce the experiment for P1-P3. However, P4-P8, involving multiple excitations become increasingly underestimated with rising binding energy. This might be due to the lack of

combination transitions in this energy region because of the limited active space. The integrated total cross sections, however, are considerably affected, being 0.30 and 0.14 a.u. for \mathbf{R}_O and $\overline{\mathbf{R}}_{O_2}$, respectively.

The oxygen molecule represents a convenient object to discuss the dependence of total decay rates on the continuum origin. Moreover, it demonstrates the largest dependence of this kind among the molecules studied here and this comparison is supported by the available experimental value. The total decay rates of the $1\pi_g$, $q-3\sigma_u$, and $d-3\sigma_u$ resonances obtained with all approaches are compiled in Table III together with the experimentally determined lifetime width of the $1\pi_g$ resonance.⁸⁹ In the literature, it has been assumed that the $1\pi_g$ and $3\sigma_u$ resonances have approximately the same decay rate.^{90,91} The computed total decay rates support this assumption for the results obtained within each model. Notably,

Table III. Computed total, doublet, and quartet autoionization rates in meV for the $1\pi_g$, $q-3\sigma_u$, and $d-3\sigma_u$ resonances of O_2 obtained with the indicated approaches. The experimental reference for the total decay width of the $1\pi_g$ resonance has been taken from Ref. 89.

	\mathbf{R}_O			$\overline{\mathbf{R}}_{O_2}$		
	$1\pi_g$	$q-3\sigma_u$	$d-3\sigma_u$	$1\pi_g$	$q-3\sigma_u$	$d-3\sigma_u$
\mathcal{H} Total	126.0	125.9	125.0	120.2	122.5	121.2
Quartet	25.2	104.8	30.2	35.7	95.6	40.6
Doublet	100.7	21.1	94.8	84.5	26.9	80.6
r^{-1} Total	169.0	167.8	165.2	186.6	187.9	184.4
Quartet	48.9	132.4	52.8	69.4	140.1	73.6
Doublet	120.1	35.4	112.4	117.2	47.8	110.8
1CA Total	69.7	65.1	65.5			
Quartet	7.5	57.5	56.0			
Doublet	62.2	7.6	9.5			
Exp. Total	149.5 \pm 10					

the total decay rates of the $q-3\sigma_u$ and $d-3\sigma_u$ resonances demonstrate the expected preferential decay into quartet and doublet target states, respectively, corresponding to their valence spin coupling. The $1\pi_g$ resonance, however, favors decay into doublet states. Interestingly, this spin selectivity is less pronounced if the $\overline{\mathbf{R}}_{O_2}$ origin is used.

In absolute terms, the \mathcal{H} coupling results recover approximately 80% of the experimental value.⁸⁹ The r^{-1} coupling in turn produces total decay rates larger than the reference by 13% and 25% for the \mathbf{R}_O and $\overline{\mathbf{R}}_{O_2}$ origins, respectively. However, the 1CA decay rates are the smallest, providing only about 45% of the experimental result. This suggests that the 1CA misses important contributions in this case. The delocalization of the core hole, that we discussed earlier, could be an explanation for this behavior, since the 1CA excludes all contributions from one atom. Still, doubling the 1CA results recovers only about 80% of the full r^{-1} coupling result at the \mathbf{R}_O origin, which is why we ascribe the remainder to non-local contributions. Although the \mathcal{H} and r^{-1} couplings reproduce the experimental reference with similar absolute deviations, see Table III, we consider the \mathcal{H} results to be in general more reliable. This is because our method does not include nuclear effects and therefore has less open decay channels. Thus it is rather likely that the present model indeed should underestimate the experimentally determined total decay rate. Further, the spectra obtained with \mathcal{H} coupling agree better with the experimental $1\pi_g$ RAES and the r^{-1} results are more sensitive to the placement of the continuum origin, see Supplement: Fig. S4.

For the $1\pi_g$ resonance (Fig. 2(b)), the computed spectrum is in an overall good agreement with experiment, with the low binding energy features R1-4 being better reproduced. This region of the spectrum corresponds predominantly to participator decay into single hole states that constitute the PES as well. The following PES and participator RAES features can be assigned to the same single hole states: P1 and R1, the high en-

ergy part of P2 and R2, P3 and R4 (30% of participator character), and P4 constitutes the rising flank of R5. The remainder of the RAES is due to spectator decay to double hole and higher excited states, the representation of which might benefit from a larger active space. For O_2 , the 1CA RAES agree quite well with those obtained with \mathcal{H} coupling, in contrast to the behavior that we found for CH_4 in Fig. 1. Further, the choice of the continuum orbital origin only weakly affects the $q-3\sigma_u$ and $d-3\sigma_u$ spectra and the overall shape of the $1\pi_g$ one. Similar to the PES spectrum, the agreement gets worse for higher binding energies. For instance, the intensity of R5 is overestimated, it is less structured, and its onset is shifted to higher energies by 1.5 eV. The atom centered approach (\mathbf{R}_O) performs better, and moreover the best agreement especially for high-energy features is obtained within the 1CA. The R6 peak behaves similar, albeit the relative overestimation by the \mathcal{H} coupling approaches, especially with $\overline{\mathbf{R}}_{O_2}$ is stronger. R7, however, is reproduced well with all approaches. Finally R8, i.e. the beginning of the tail region appears blue shifted by 2.5 eV. The intensity overestimation with the $\overline{\mathbf{R}}_{O_2}$ origin is due to the enhancement of the quartet decay branch, as indicated by the total decay rates in Table III.

For the $3\sigma_u$ resonance the agreement with the experiment is worse than for the $1\pi_g$ resonance. The $q-3\sigma_u$ and $d-3\sigma_u$ RAES appear to be shifted with respect to each other both due to exchange splitting in the core-excited states and preferential decay to different spin manifolds of O_2^+ . In particular, the $q-3\sigma_u$ spectrum is shifted to lower binding energies by ~ 2.5 eV relative to the experiment even after the alignment of all spectra to the reference IPs, see Table II. Further, the intensity of the features with a binding energy above 35 eV (S4-6) are considerably underestimated. This discrepancy may be attributed mainly to two reasons as discussed previously in experimental works.^{85,90,91,93} As mentioned before, the $3\sigma_u$ band is overlaid by a manifold of Rydberg transitions in addition to the exchange splitting between $q-3\sigma_u$ and $d-3\sigma_u$ resonances.⁸⁵ Namely, within the excitation bandwidth of 2.7 eV,⁵⁸ Rydberg states of $np(\pi_u)$, $n = 3-7$ and $ns(\sigma_g)$, $n = 3-5$ character have been identified by Ma et al.⁸⁵ around 540 eV. This indicates that the measured spectrum contains contributions from all these resonances and in our calculation we consider only one at a time. Further, the $3\sigma_u$ states are dissociative and a fast bond elongation is expected to occur on the timescale of the Auger decay that has been claimed to lead to appearance of atomic features.^{58,90,91} Our test calculations with a bond distance of 1.26 Å (0.05 Å elongation) show for $q-3\sigma_u$ an almost doubled energetic mismatch between theory and experiment of 4.5 eV (compare with 2.5 eV), indicating that a simple bond elongation might not explain the effect. To close this question, the one-step model for resonant Auger decay¹⁹ has to be employed together with a larger active space that includes excitations to Rydberg orbitals. Finally, varying the excitation ratio of all these resonances might strongly influence the

result.

Summarizing, the total Auger decay rates, the $1\pi_g$ RAES as well as the PES are in quite good agreement with the experiment, whereas the $3\sigma_u$ RAES agrees slightly worse calling for more sophisticated treatment. In general, the full \mathcal{H} coupling seems to yield the most stable spectra and total decay rates and the 1CA predicts spectra of the same quality as the full approaches, although the overall decay rates are underestimated. Finally, the choice of the continuum origin has no strong effect on the spectra and total decay rates, although the total photoionization cross sections vary by a factor of two.

C. Nitrogen dioxide

NO_2 , being a radical with multi-configurational character of the ground doublet state, represents an increase of complexity with respect to O_2 . This fact makes it a convenient object to study the performance of our multi-reference protocol. Moreover, recent reference data for its XAS^{94,96}, PES⁹⁵, and RAES⁹⁵ taken at the nitrogen and oxygen K-edges are available for comparison. In this article, we focus on the nitrogen K-edge. This takes advantage of the fact that the origin of the spherically symmetric continuum functions can be unambiguously put on the nitrogen atom \mathbf{R}_N .

a. XAS The calculated XAS at the nitrogen K-edge of NO_2 is presented in Fig. 3 panel (a), together with the experimental reference that has been digitized from Gejo et al.⁹⁴ Both spectra have been normalized to the height of the $2b_1$ peak. The relative intensities of the $6a_1$ and $2b_1$ resonances are reproduced almost exactly, although the $6a_1$ peak is predicted slightly by 0.2 eV too high in energy. The features at higher energies correspond to excitations to the $7a_1$, $5b_2$, and Rydberg orbitals⁹⁴ that are not included in our active space. Thus, they are reproduced herein only to some extent.

The excitation energies of 402.86 eV and 403.73 eV used to obtain the RAES from the low and high energy flank of the $2b_1$ resonance⁹⁵ are indicated by the arrows. We have connected them to the positions of two core-excited states predicted by our calculations that correspond to the $2b_1$ resonance. Our calculation predicts a splitting of 0.34 eV for these states. Further, the oscillator strength obtained for the lower state is a factor of ~ 20 smaller than the one of the higher state. An analysis in terms of the occupation numbers of the state averaged orbitals obtained from the CASSCF procedure shows that both states are quite similar in character, bearing the $\text{N}(1s)$ core hole and the excitation to the $2b_1$ orbital. However, the analysis of the core-hole spin in our calculations does not support the assignment of this splitting to an exchange mechanism, in contrast to the experimental results for the $\text{O}(1s) \rightarrow 2b_1$ resonance.⁹⁵

b. PES and RAES Panel (b) comprises the RAES corresponding to the low and high energy flanks of the

$2b_1$ resonance, as well as the direct PES taken at 399 eV below the edge. The experimental data has been digitized from Ref. 95. The PES and RAES have been normalized to the peaks 4 and 3, respectively. To converge the partial decay rates and the ionization cross sections it was necessary to include partial waves up to $l_{\text{max}} = 9$ (r^{-1} coupling) and $l_{\text{max}} = 4$ (1CA) as well as $l_{\text{max}} = 15$ (PES), respectively. Note that we have used a Lorentzian line-shape with an Full Width at Half Maximum (FWHM) of 0.1 eV for peak 6 in the calculated PES. To have a common reference, the theoretical and experimental data have been aligned to reference values for the lowest singlet and triplet IPs as detailed in Table II. For the sake of clarity a common set of identifiers 1-7 is used for features in all spectra. The dashed lines denote features or groups thereof that predominantly correspond to direct photoionization, whereas those that are found in both, PES and RAES, are indicated with solid lines.

PES is found to be in fairly good agreement with experiment, although the feature 2 is overestimated by an approximate factor of 2. Further, the peak 4 is slightly overestimated and around 23.6 eV our simulation yields a feature that has no correspondence in the experimental data. Some of these deviations might be due to anisotropy effects present in the experimental data⁹⁵ which are not recovered in our angle integrated spectra. In addition, the valence PES is a rather non-local probe and thus might be more sensitive to the quality of the continuum orbital than RAES, which in this case seems to be an almost purely local process. An improvement could thus require a more elaborate model for the continuum electron, possibly involving a multi-centered approach.²⁴

We address here different flanks of the $2b_1$ resonance which exhibits an exchange splitting of ~ 0.5 eV for the $\text{O}(1s)$ hole^{94,95}. Piancastelli et al.⁹⁵ found that the low energy side of the $\text{O}(1s) \rightarrow 2b_1$ resonance favors decay to triplet ionized states whereas the higher energy side favors decay to singlet states, which is a trace of this splitting. A similar behavior can be expected for the $\text{N}(1s) \rightarrow 2b_1$ resonance, although the splitting is assumed to be smaller⁹⁵. However, to the best of our knowledge no data regarding the splitting has been published yet and the experimental RAES results in Ref. 95 are inconclusive in this case. We attempt to shed light on this question in the following.

The results of the r^{-1} coupling are presented in Fig. 3 assuming the full molecular treatment and 1CA. Noteworthy, the RAES obtained within the 1CA closely resemble the ones that have been obtained by taking into account non-local contributions from the oxygen atoms as well. Adding to that, the calculated total decay widths of 92 meV and 98 meV corresponding to the 1CA and the full r^{-1} couplings agree with each other as opposed to oxygen case. Thus it seems that the decay of the $1b_2$ resonance can be described quite well as a purely local phenomenon, in contrast to our findings for CH_4 and O_2 .

To unravel the relative contribution of the triplet and singlet decay pathways, we found T:S ratios of 1.0 and

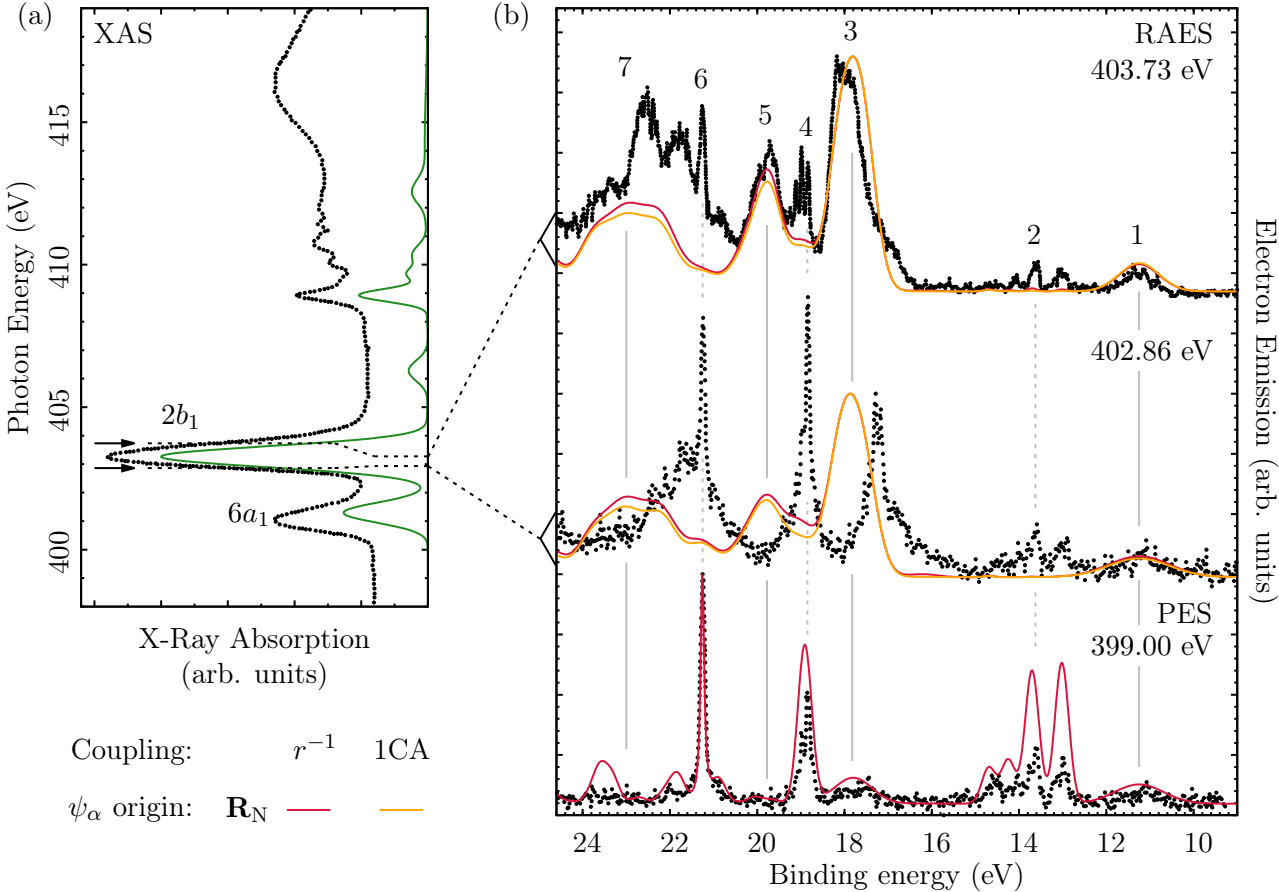


Figure 3. (a) Theoretical nitrogen K-edge XAS of NO_2 (green, solid) and the experimental reference digitized from Gejo et al.⁹⁴ (black, dotted). The arrows indicate the excitation energies used by Piancastelli et al.⁹⁵ to obtain the experimental RAES in panel (b). In addition, the dashed lines link the experimental excitations to the respective core-excited states predicted in our calculation and the corresponding RAES in (b). Therein, the decay spectra measured at the low and high energy sides of the $2b_1$ resonance as well as the PES taken at 399 eV below the edge⁹⁵ (dotted) are compared against our theoretical results (solid). The partial decay rates have been obtained using r^{-1} coupling and the 1CA. The vertical lines indicate corresponding features that are predominantly found in PES (dashed) and RAES (solid), respectively. The applied shifts and broadenings are detailed in Table II and in Supplement: Table S3.

1.2 for the the low and high energy $1b_2$ RAES. Thus there is no appreciable difference in the spin coupling of the respective core-excited states, supporting the result from the analysis of the respective core-hole spins, see the discussion of the XAS above. In contrast, the total photoionization cross section yields a T:S ratio of 2.5, i.e., the PES at this energy is dominated by the triplet branch. This behavior fits well with the fact that the $6a_1$ orbital is occupied in the NO_2 ground state, as well as in a large part of the triplet ionized states but only to lesser extent in the singlet states.

Concerning the analysis of the spectra, the comparison against the reference data⁹⁵ yields a very good agreement regarding the energetic positions of all features in the high energy RAES and the PES. The peaks 2, 4, and 6 are predominant PES features and their presence in the experimental RAES indicates that a considerable portion of the absorbed photon flux leads to a direct

ionization rather than to a resonant excitation of the molecule. To reproduce these effects theoretically, the one-step model¹⁹ for resonant Auger decay must be employed.

The frontier orbital configurations for NO_2 as well as singlet and triplet NO_2^+ are $4b_2^2 1a_2^2 6a_1^1$, $4b_2^2 a_2^2 6a_1^0$, and $1a_2^2 4b_2^1 6a_1^1$, respectively. The $2b_1$ orbital however, is unoccupied in all ground states with given charge and multiplicity. Hence, core excitations to the $2b_1$ orbital can be expected to have a considerable participator decay contribution. In contrast, the peaks 3, 5, and 7 are predominant spectator Auger decay contributions having only small counterparts in the PES. Finally, the lowest energy peak, 1, corresponds to the singlet NO_2^+ ground state, i.e. the $16a_1^{-1}$ ionization. It can be reached via direct ionization and participator decay of the $2b_1$ resonance and contributes equally to both, PES and RAES. In opposite to that, participator decay into the higher

lying single hole states contained in feature 2, i.e., $^34b_2^{-1}$, $^31a_2^{-1}$, $^11a_2^{-1}$, and $^14b_2^{-1}$ at 13 eV, 13.6 eV, 14.2 eV, and 14.6 eV, is suppressed, although these states contribute to the PES. We can confirm the statement of Ref. 95 that this is most likely due to the localization of the $1a_2$ and $4b_2$ orbitals on the oxygen atoms, whereas the $2b_1$ excitation is primarily localized on the nitrogen. Hence, the main part of the Auger decay of the $2b_1$ resonance at the N K-edge of NO_2 can be ascribed to spectator decay into double-hole or higher excited states, which appear only as satellites in the PES. This is a common situation and underlines the importance of the joint analysis of PES and RAES. The strong configuration mixing in the electronic structure calculation hinders a clear assignment of the remaining features, thus, we refer to the assignments in Refs. 97 and 76.

One can expect the Auger features to shift on the binding energy scale when changing the photon energy, the energetic position of the direct ionization PES features, however, should stay intact. The theoretically obtained RAES taken at the low-energy flank is rather similar to our high-energy result and does not recover the shift of the decay features 3, 5, and 7 by approximately 0.6 eV observed in the experimental spectrum. Judging by the relative contribution of the direct ionization (PES) features 2, 4, and 6 to the measured data, the resonant decay contribution is here much weaker than in the RAES taken at high-energy flank. In turn, feature 1 can be ascribed exclusively to direct photoionization that does not appear red-shifted in contrast to its participator decay counterpart that could be concealed within the noise due to its small intensity. Since our preliminary studies with a larger active space and basis set have not led to an improvement here, we tend to attribute this shift to difference in exciting photon energies and vibrational effects. Nevertheless, we do not exclude other possible explanations.

Finally, concerning the relative intensities. The overall agreement is good, with some exclusions. For instance in the high energy flank RAES, the relative intensities of the features 1, 3, and 5 are reproduced quite well, while the peak 7 is underestimated considerably and is less structured than in experiment. The situation is more delicate concerning the low energy RAES. In this case, the overall small magnitude of the decay features in the experimental spectrum could be due to the low oscillator strength of the corresponding core-excited state, as discussed in the XAS part. Further, the red shift of the resonant decay features by 0.6 eV increases the overlap between the direct photoionization peaks 4 and 6 with the decay features 5 and 7, respectively. Thus a disentanglement of direct and resonant contributions is hardly possible for these peaks. It seems that for a better reproduction of the experimental results for the low energy RAES, the one-step ansatz to RAES, allowing for interference between multiple resonant decay and direct ionization channels¹⁹ as well as the inclusion of vibrational effects have to be considered.

In summary, the comparison to the experimental XAS has verified that our electronic structure is suitable to describe the $2b_1$ resonance at the nitrogen K-edge. Further, our theoretical data agree well with the experimental reference for the PES and the RAES recorded at the high energy flank of the resonance. In addition, the 1CA results closely resemble the spectra and total decay rates obtained when all atomic centers are included. However, the RAES stemming from the low energy side of the resonance probably requires a more involved treatment of the resonance decay within the one-step model as well as the inclusion of nuclear effects. Finally, our results do not indicate a difference in the spin coupling on the low and high energy flank of the $\text{N}(1s) \rightarrow 2b_1$ resonance, in contrast to previous findings for the $\text{O}(1s) \rightarrow 2b_1$ resonance.⁹⁵

D. Pyrimidine

Finally, we benchmark the SCI approach for the pyrimidine molecule ($\text{C}_4\text{H}_4\text{N}_2$). Having six heavy atoms arranged in a C_{2v} symmetric ring, the theoretical study of its PES and RAES is considerably more involved than for the previous examples. Moreover, pyrimidine is interesting on its own, since the structures of the nucleic acids uracil, cytosine, and thymine are derived from it. Its ionization spectra are thus an important landmark on the route towards a better understanding of DNA radiation damage. Due to this, a number of experimental and theoretical investigations regarding its XAS^{77,98}, PES^{77,99-102}, normal¹⁰³ and resonant⁷⁷ Auger emission have been published during the last 20 years. Bolognesi et al.⁷⁷ have recently reported complete sets of XAS, PES, and RAES measurements at the carbon and nitrogen K-edges of pyrimidine, making this work a suitable reference for our simulations. Conveniently, the electrons have been collected at the pseudo magic angle, suppressing angular anisotropy effects.

We have chosen to focus on the nitrogen K-edge of pyrimidine, since the corresponding RAES are quite structured and it allows to incorporate only two instead of four core orbitals into the active space. However, the symmetric arrangement of the nitrogen atoms, Fig. 4, might lead to core-hole delocalization effects. Similar to the O_2 case, see Sec. IV B, the continuum orbital origin is also not well defined. Here, two options seem reasonable. First, it might be placed on one of the nitrogen atoms, denoted as \mathbf{R}_N , or in the geometric center of the ring, $\overline{\mathbf{R}}_{\text{C}_4\text{N}_2}$, which might be the most balanced choice if all atoms contribute to the continuum orbital.

a. XAS The calculated nitrogen K-edge XAS of pyrimidine is depicted in panel (a) of Fig. 4 together with the experimental reference;⁷⁷ the band labels are taken from this experiment. In case of pyrimidine, the agreement with the experimental XAS is less satisfactory than for the other molecules. In accord with previous findings,^{77,104} we assign the main features to a $\pi^*(a_2)$ core

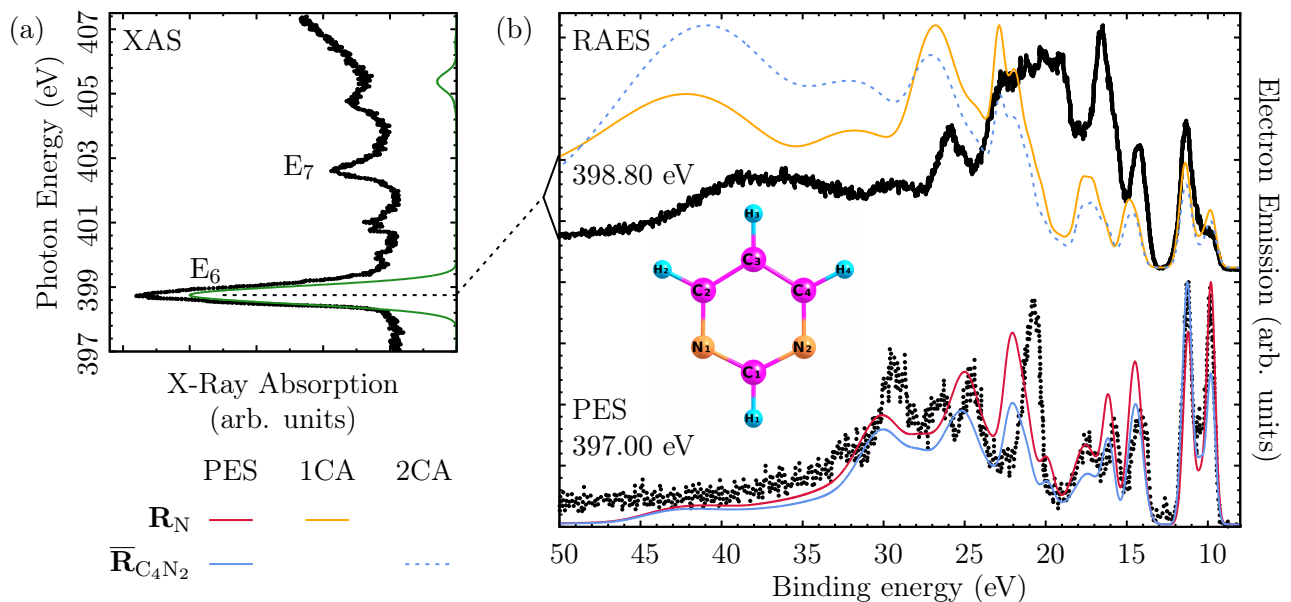


Figure 4. (a) Theoretical nitrogen K-edge XAS of pyrimidie (solid green) and the respective experimental measurement taken from Bolognesi et al.⁷⁷ (black dotted). (b) Theoretical and experimental⁷⁷ (black) RAES of the E6 resonance and the pre-edge PES obtained at the indicated energies. The continuum orbitals have been evaluated using the $V_f^J(r)$ potential centered at one nitrogen atom, \mathbf{R}_N , or at the geometric center of the ring, $\bar{\mathbf{R}}_{C_4N_2}$. The RAES have been evaluated in the 1CA and 2CA, see text. The applied shifts and broadenings are detailed in Table II and Supplement: Table S4, respectively.

excitation (E6) and to transitions to the π - Rydberg mixed $\pi^{\text{Ryd}}(b_1)$ orbitals (~ 406 eV; E7). In contrast, the shoulder of E6 at 399.9 eV that has been attributed to $\pi^*(b_1)$ excitations¹⁰⁴ is missing in our results. In fact, the corresponding core-excited state is present at 400.4 eV, but its absorption is by a factor of ~ 500 lower than for the E6 one. A different theoretical study,⁹⁸ however, found this feature to be underestimated as well, but perceivable. Finally, the structure around 401 eV has been attributed to a contamination with N_2 molecules¹⁰⁴ and can be neglected in the discussion.

The energetic spacing between E6 and E7 is overestimated by about 2.8 eV in our calculations. This is an indication of the lack of electron correlation as well as Rydberg character in the active orbitals. However, including a higher level of CI and employing much larger Rydberg bases has not been feasible.

b. PES and RAES The predicted PES at 397 eV and the RAES obtained at the E6 resonance together with experimental data digitized from Bolognesi et al.⁷⁷ are compiled in Fig. 4 (b). All spectra have been normalized to their respective highest peaks. We focus here solely on the E6 resonance, because its spectrum yields more structure than the E7 one⁷⁷ and we deem our core-excited states to be more reliable for this lower lying resonance. The continuum orbitals used in the calculations have been constructed based on the $V_f^J(r)$ potential centered at the \mathbf{R}_N and $\bar{\mathbf{R}}_{C_4N_2}$ origins, as depicted in Fig. 4. Due to the computational costs, the RAES have only been obtained in the nitrogen centered 1CA, as well as

the Two-Center Approximation (2CA). For the latter spectrum contributions from at most two different atoms of the C_4N_2 ring have been included in a two-center approximate fashion with the continuum orbitals being centered at $\bar{\mathbf{R}}_{C_4N_2}$. We have included partial waves up to $l_{\text{max}} = 15$ for the PES and 2CA RAES, which is the current maximum supported by our code. However, the contributions of the $l = 15$ term can for some transitions reach up to 15% and 25% for the $\bar{\mathbf{R}}_{C_4N_2}$ (PES and 2CA RAES) and \mathbf{R}_N (PES) origins, respectively. Hence, partial waves with higher angular momenta might be needed to ensure complete convergence of the respective band intensities. However, for the 1CA decay spectrum, corresponding to the autoionization contribution from one nitrogen atom embedded in the molecular potential, the intensities converged already for $l = 4$, although $l_{\text{max}} = 9$ has been used.

At first glance, our simulations reproduce the experimental PES results very well, whereas the RAES intensities are matched to a lesser extent. For the detailed discussion, we follow Bolognesi et al.⁷⁷ in dividing the spectra into three regions, spanning binding energies up to 13 eV (1), 20 eV (2), and > 20 eV (3). We begin the discussion with the PES. Region (1) contains clearly distinguishable single hole states with the leading configurations $n_{N_-}(7b_2)^{-1}$ at 9.8 eV, $\pi_3(2b_1)^{-1}$ at 10.5 eV, $n_{N_+}(11a_1)^{-1}$ at 11.2 eV and $\pi_2(1a_2)^{-1}$ at 11.5 eV in Fig. 4 (b). This assignment agrees with the one obtained in Refs. 99,100, regarding the still controversial question of the ordering of the $n_{N_+}(11a_1)^{-1}$ and $\pi_2(1a_2)^{-1}$ fea-

tures⁷⁷ that are difficult to resolve experimentally. The region (2), marks the transition from single to double hole states. The feature around 14.5 eV comprises three states of dominant $\pi_1(1b_1)^{-1}$, $\sigma(10a_1)^{-1}$ and $\sigma(6b_2)$ nature with an admixture of up to 20% π^* character. The other two peaks, correspond dominantly to lower lying σ^{-1} states with up to 30% π^* character. Finally, in region (3), the density of the ionized states increases considerably and they are predominantly of two hole character. Here, multiple transitions contribute to each peak and an assignment in terms of orbitals is not possible anymore.

Concerning the intensities, in region (1), the height ratio of the double peak is not symmetric. The low and high energy parts are enhanced with the \mathbf{R}_N and $\overline{\mathbf{R}}_{C_4N_2}$ origins, respectively. In region (2), $\overline{\mathbf{R}}_{C_4N_2}$ leads to a better agreement for the first two peaks, whereas using \mathbf{R}_N resembles the part around 17.5 eV better. The experimental data in region (3) yields four distinct features around 21 eV, 25 eV, 26.5 eV, and 29.5 eV as well as an unresolved tail at higher energies. Our data reproduces the general structure, albeit the features appear blue shifted by 1.3 eV, 0.5 eV, 1.1 eV, and 0.8 eV, respectively. Further, the relative intensity of this region tends to be underestimated, in particular with the $\overline{\mathbf{R}}_{C_4N_2}$ origin. Especially the feature around 27.5 eV appears only as a small shoulder. Since the PES of O₂ demonstrated only minor variations for different origins, one might attribute the deviations observed here to the fact that the angular momentum expansion is not fully converged in this case.

Now concerning the RAES of the E6 resonance, Fig. 4 (b). Both, the 1CA and 2CA spectra show only a very approximate correspondence to the experimental data. In region (1) the theoretical RAES resembles the shape of the experimental reference. It can be assigned to pure participator decay into the single hole states that constitute the PES in this region as well. Already in region (2), we find that spectator decay is dominating and the number of final states increases to around 40 for the whole region. Here, our data yields two distinct peaks similar to the experimental result, but blue shifted by about 0.7 eV. The relative intensity of the one at 17.5 eV, which is the most prominent feature in the experimental data, however, is underestimated by a factor of 2.5 in the 1CA. Finally, region (3) comprises more than 250 mainly spectator transitions with appreciable intensities that in total constitute the spectrum. Here, the experimental data comprises 4 features. A broad one (19.0 – 24.0 eV) is only partially reproduced in the theoretical spectrum. It is too narrow, spanning only 21.5 – 23.5 eV and its rising edge is blue shifted by approximately 3.0 eV. Next, a narrower peak around 26.0 eV is found in our data with a blue shift of 0.5 eV but too large in intensity. Furthermore, the two broad features around 29.0 eV and 37.0 eV in the experiment are represented with respective blue shifts of 3.0 eV and 5.0 eV. Generally, the tail region, > 25.0 eV carries too much intensity in our calculation, especially in the 2CA variant.

In comparison to our RAES results for O₂ and NO₂, we find the extent of the disagreement between the theoretical and experimental decay spectra surprising. This is especially striking, since the PES is represented quite well by our approach, indicating that the valence electronic structure of the cation is well described with the present active space and that the employed continuum model captures the most important effects. Unfortunately, a detailed scrutinization of this deviation is difficult since, to the best of our knowledge, references obtained on a higher level of theory are not available. Tentatively, the disagreement can be assigned to the exclusion of the hydrogen atoms within both, 1CA and 2CA, which might induce a similar characteristic as for methane, see Fig. 1. This line of argumentation is supported by the fact that region (2), with the greatest mismatch to the experimental reference, comprises ionized states bearing holes in the σ valence orbitals which contain a considerable hydrogen character. Further, the 2CA ansatz, that includes all “heavy” atoms does not improve the agreement with the experimental data in this region, although the total decay rates increase by a factor of 3.5 from 32.5 meV (1CA) to 114.7 meV (2CA). While this indicates that non-local contributions from the C and N atoms play a considerable role for the decay of the E6 resonance, it also shows that the inclusion of the hydrogen atoms might be necessary, to further improve the spectrum. Another reason could be that the active space used herein does in fact not describe the core-excited states well enough, as pointed out in the discussion of the XAS.

We conclude the discussion of this system with the following recapitulation. The pyrimidine molecule has been studied with a large active space, allowing one electron to be removed from the N(1s) orbitals, as well as a single electron to be excited into 8 valence orbitals. With this active space not all prominent XAS features can be reproduced. However, irrespective of the continuum orbital origin, the experimental PES has been reproduced quite well with the SCI approach, although it is not fully converged at $l_{\max} = 15$. This also indicates that the valence electronic structure is described sufficiently accurate. Still, the simulated RAES of the E6 resonance obtained with our approach yield notable differences to the experimental reference⁷⁷ in the spectator decay region. We tentatively ascribe this to the exclusion of the hydrogen atoms within the employed 1CA and 2CA schemes, which might influence different spectral regions to a varying degree, thus altering the shape of the spectrum. Further studies including the hydrogen orbitals as well as involving an active space that covers more core-hole correlation need to be carried out to rule out these remaining uncertainties.

V. CONCLUSIONS AND OUTLOOK

In this article, we have presented the SCI approach for the evaluation of photoionization cross sections and

partial Auger decay rates for the case of molecules. It is a logical continuation of our previous benchmark of the protocol for the atomic case of RAES of the neon $1s^{-1}3p$ resonance, where it was shown to yield spectra and total decay rates in good agreement with experimental references.⁵⁵ The central approximation in the protocol is that the angular structure of the molecular potential is averaged out, leading to spherically symmetric continuum orbitals that are obtained by numerically solving the radial Schrödinger equation. As has been shown here, such an approach, being natural for atoms, in fact provides a valuable insight into the nature of molecular photoionization and autoionization spectral features as well.

The investigated molecules have been selected to represent different classes. To perform a thorough test of the protocol, the XAS, PES, and RAES at the carbon, oxygen and nitrogen K-edges of CH₄, O₂, and NO₂ as well as pyrimidine, respectively, have been evaluated and compared to the experimental data. Of course, accurate calculations of these molecules in the gas phase require the inclusion of vibrational effects, with the O₂ $3\sigma_u$ resonance being an extreme case. Here, they have been excluded and the discussion is focused on the purely electronic effects.

From the viewpoint of electronic structure calculations, this protocol can be applied together with any quantum chemistry method, allowing for a CI-like representation of the wave function. In particular, in the present article the bound electronic structure is obtained at the RASSCF/RASPT2 level. The analysis of the XAS has shown that this method with the respective active spaces is capable of capturing the most important effects in core-excited states of neutral systems with the exception of pyrimidine, possibly requiring a larger active space. Further, the energetic positions of lines in PES and RAES, characterizing the structure of the valence levels of the ionized system could be reproduced with an overall high accuracy. However, there is a tendency to overestimate the binding energies towards high-energy parts of the spectra.

Regarding the PES intensities, the SCI approach has lead to fairly good agreement with experiments for NO₂, pyrimidine, and the lower binding energy region of O₂, but in some cases discrepancies have been observed. For example, the high binding energy region of the O₂ PES bears too few intensity, which we attribute to the lack of combination transitions to Rydberg orbitals in the active space. In CH₄, the relative intensities of the a_1^{-1} and t_2^{-1} peaks PES at 282.2 eV can not be correctly described using our approach.

The SCI approach appears to produce in general reasonable RAES, for all resonances in methane, the $1\pi_g$ resonance of O₂, and the high-energy flank of the $2b_1$ resonance in NO₂. Those spectra which cannot be accurately reproduced generally correspond to cases when either vibronic effects are important, several resonances are overlaying, or the active space is too small. Nevertheless, this information can be still valuable for the

assignment of experimental spectra.

The \mathcal{H} coupling has been applied only to CH₄ and O₂, where it has led to the best agreement. However, the approximate r^{-1} coupling produces very similar spectra for CH₄, whereas for O₂ the differences between both couplings are larger. Overall, the origin dependence of the spectra in both O₂ and pyrimidine cases has been found to be relatively small, especially when \mathcal{H} coupling is applied. The One-Center Approximation (1CA) seems to be not applicable in all cases for the present method. Although it is very attractive from the computational viewpoint as it substantially reduces the numerical effort. For example, the CH₄ 1CA results do not agree well to experiment, while for NO₂ they closely resemble the r^{-1} ones. However, for pyrimidine only the 1CA and 2CA, including two-center contributions from only heavy atoms, were feasible. Unfortunately, these approximations do not lead to good agreement with experiment in this case; we suppose that the deviations can be rather attributed to deficiencies of the quantum chemistry setup, exclusion of hydrogen contributions, or the SCI model itself.

Finally, some of the deviations between calculations and experiment can be mitigated if the one-step model is applied. This might be especially needed to describe spectral regions with notable participator decay character and cases with strong interference between different ionization pathways. Taking into account nuclear motion might also be highly advisable.

ACKNOWLEDGMENTS

Financial support from the Deutsche Forschungsgemeinschaft Grant No. BO 4915/1-1 is gratefully acknowledged.

REFERENCES

- ¹A. Stolow, A. E. Bragg, and D. M. Neumark, *Chem. Rev.* **104**, 1719 (2004).
- ²S. Hofmann, *Auger- and X-Ray Photoelectron Spectroscopy in Materials Science: A User-Oriented Guide*, Springer Series in Surface Sciences No. 49 (Springer, Heidelberg, New York, 2013).
- ³S. Hüfner, *Photoelectron Spectroscopy: Principles and Applications* (Springer, Berlin, Heidelberg, 2003).
- ⁴D. Yepes, R. Seidel, B. Winter, J. Blumberger, and P. Jaque, *J. Phys. Chem. B* **118**, 6850 (2014).
- ⁵R. Golnak, S. I. Bokarev, R. Seidel, J. Xiao, G. Grell, K. Atak, I. Unger, S. Thürmer, S. G. Aziz, O. Kühn, B. Winter, and E. F. Aziz, *Sci. Rep.* **6**, 24659 (2016).
- ⁶S. I. Bokarev and O. Kühn, *Wiley Interdiscip. Rev. Comput. Mol. Sci.*, e1433 (2019).
- ⁷H. Wang, T. Möhle, O. Kühn, and S. I. Bokarev, *Phys. Rev. A* **98**, 013408 (2018).
- ⁸A. Rudenko, L. Inhester, K. Hanasaki, X. Li, S. J. Robotjazi, B. Erk, R. Boll, K. Toyota, Y. Hao, O. Vendrell, C. Bomme, E. Savelyev, B. Rudek, L. Foucar, S. H. Southworth, C. S. Lehmann, B. Kraessig, T. Marchenko, M. Simon, K. Ueda, K. R. Ferguson, M. Bucher, T. Gorkhover, S. Carron, R. Alonso-Mori, J. E. Koglin, J. Correa, G. J. Williams, S. Boutet, L. Young,

- C. Bostedt, S.-K. Son, R. Santra, and D. Rolles, *Nature* **546**, 129 (2017).
- ⁹I. Unger, R. Seidel, S. Thürmer, M. N. Pohl, E. F. Aziz, L. S. Cederbaum, E. Muchová, P. Slavíček, B. Winter, and N. V. Kryzhevoi, *Nat. Chem.* **9**, 708 (2017).
- ¹⁰V. Stumpf, K. Gokhberg, and L. S. Cederbaum, *Nat. Chem.* **8**, 237 (2016).
- ¹¹P. Slavíček, N. V. Kryzhevoi, E. F. Aziz, and B. Winter, *J. Phys. Chem. Lett.* **7**, 234 (2016).
- ¹²R. W. Howell, *Int. J. Radiat. Biol.* **84**, 959 (2008).
- ¹³A. Yokoya and T. Ito, *Int. J. Radiat. Biol.* **93**, 743 (2017).
- ¹⁴M. Nisoli, P. Decleva, F. Calegari, A. Palacios, and F. Martín, *Chem. Rev.* **117**, 10760 (2017).
- ¹⁵T. Åberg, G. Howat, L. Karlsson, J. A. R. Samson, H. Siegbahn, and A. F. Starace, *Corpsucles and Radiation in Matter I*, edited by W. Mehlhorn, Encyclopedia of Physics, Vol. 31 (Springer, Berlin, 1982).
- ¹⁶A. F. Starace, in *Corpsucles and Radiation in Matter I*, Encyclopedia of Physics, Vol. 31, edited by W. Mehlhorn and W. Mehlhorn (Springer, Berlin, 1982) pp. 1–121.
- ¹⁷U. Fano, *Physical Review* **124**, 1866 (1961), 10750.
- ¹⁸G. Breit and H. A. Bethe, *Phys. Rev.* **93**, 888 (1954).
- ¹⁹T. Åberg and G. Howat, in *Corpsucles and Radiation in Matter I*, Encyclopedia of Physics, Vol. 31, edited by W. Mehlhorn (Springer, Berlin, 1982) pp. 469–619.
- ²⁰P. G. Burke, *R-Matrix Theory of Atomic Collisions: Application to Atomic, Molecular and Optical Processes*, Springer Series on Atomic, Optical, and Plasma Physics No. 61 (Springer, Heidelberg, 2011).
- ²¹H. Bachau, E. Cormier, P. Decleva, J. E. Hansen, and F. Martín, *Rep. Prog. Phys.* **64**, 1815 (2001).
- ²²R. Colle and S. Simonucci, *Phys. Rev. A* **39**, 6247 (1989).
- ²³R. Colle and S. Simonucci, *Phys. Rev. A* **48**, 392 (1993).
- ²⁴C. Marante, M. Klinker, I. Corral, J. González-Vázquez, L. Argenti, and F. Martín, *J. Chem. Theor. Comput.* **13**, 499 (2017).
- ²⁵F. Martín, *J. Phys. B At. Mol. Opt. Phys.* **32**, R197 (1999).
- ²⁶R. Colle, D. Embriaco, M. Massini, S. Simonucci, and S. Taioli, *J. Phys. B At. Mol. Opt. Phys.* **37**, 1237 (2004).
- ²⁷M. Klinker, C. Marante, L. Argenti, J. González-Vázquez, and F. Martín, *Phys. Rev. A* **98**, 033413 (2018).
- ²⁸D. Toffoli, M. Stener, G. Fronzoni, and P. Decleva, *Chemical Physics* **276**, 25 (2002).
- ²⁹D. Catone, M. Stener, P. Decleva, G. Contini, N. Zema, T. Proserpi, V. Feyrer, K. C. Prince, and S. Turchini, *Phys. Rev. Lett.* **108**, 083001 (2012).
- ³⁰M. Stener, D. Toffoli, G. Fronzoni, and P. Decleva, *Theor Chem Account* **117**, 943 (2007).
- ³¹F. Calegari, D. Ayuso, A. Trabattoni, L. Belshaw, S. D. Camillis, S. Anumula, F. Frassetto, L. Poletto, A. Palacios, P. Decleva, J. B. Greenwood, F. Martín, and M. Nisoli, *Science* **346**, 336 (2014).
- ³²E. Plésiat, S. E. Canton, J. D. Bozek, P. Decleva, and F. Martín, *J. Phys. Chem. A* **123**, 1062 (2019).
- ³³P. V. Demekhin, D. V. Omel'yanenko, B. M. Lagutin, V. L. Sukhorukov, L. Werner, A. Ehresmann, K.-H. Schartner, and H. Schmoranzner, *Opt. Spectrosc.* **102**, 318 (2007).
- ³⁴P. V. Demekhin, I. D. Petrov, V. L. Sukhorukov, W. Kielich, P. Reiss, R. Hentges, I. Haar, H. Schmoranzner, and A. Ehresmann, *Phys. Rev. A* **80** (2009).
- ³⁵H. I. B. Banks, D. A. Little, J. Tennyson, and A. Emmanouilidou, *Phys. Chem. Chem. Phys.* **19**, 19794 (2017).
- ³⁶H. Siegbahn, L. Asplund, and P. Kelfve, *Chem. Phys. Lett.* **35**, 330 (1975).
- ³⁷F. P. Larkins, L. C. Tulea, and E. Z. Chelkowska, *Aust. J. Phys.* **43**, 625 (1990).
- ³⁸R. Fink, *J. Electron Spectrosc. Relat. Phenom.* **76**, 295 (1995).
- ³⁹O. Travnikova, R. F. Fink, A. Kivimäki, D. Céolin, Z. Bao, and M. N. Piancastelli, *Chem. Phys. Lett.* **474**, 67 (2009).
- ⁴⁰L. Inhester, K. Hanasaki, Y. Hao, S.-K. Son, and R. Santra, *Phys. Rev. A* **94**, 023422 (2016).
- ⁴¹Y. Hao, L. Inhester, K. Hansaki, and R. Santra, *Struct. Dyn.* **2**, 041707 (2015).
- ⁴²C. M. Oana and A. I. Krylov, *J. Chem. Phys.* **131**, 124114 (2009).
- ⁴³C. M. Oana and A. I. Krylov, *J. Chem. Phys.* **127**, 234106 (2007).
- ⁴⁴G. Grell, S. I. Bokarev, B. Winter, R. Seidel, E. F. Aziz, S. G. Aziz, and O. Kühn, *J. Chem. Phys.* **143**, 074104 (2015).
- ⁴⁵B. Mignolet, J. O. Johansson, E. E. B. Campbell, and F. Remacle, *ChemPhysChem* **14**, 3332 (2013).
- ⁴⁶A. O. Gunina and A. I. Krylov, *J. Phys. Chem. A* **120**, 9841 (2016).
- ⁴⁷T. Möhle, O. S. Bokareva, G. Grell, O. Kühn, and S. I. Bokarev, *J. Chem. Theor. Comput.* **14**, 5870 (2018).
- ⁴⁸A. Mognilevski, M. Wilke, G. Grell, S. I. Bokarev, S. G. Aziz, N. Engel, A. A. Raheem, O. Kühn, I. Y. Kiyani, and E. F. Aziz, *ChemPhysChem* **18**, 465 (2017).
- ⁴⁹A. A. Raheem, M. Wilke, M. Borgwardt, N. Engel, S. I. Bokarev, G. Grell, S. G. Aziz, O. Kühn, I. Y. Kiyani, C. Merschjann, and E. F. Aziz, *Struct. Dyn.* **4**, 044031 (2017).
- ⁵⁰V. Carravetta, H. Ågren, O. Vahtras, and H. J. A. Jensen, *J. Chem. Phys.* **113**, 7790 (2000).
- ⁵¹K. Gokhberg, V. Vysotskiy, L. S. Cederbaum, L. Storchi, F. Tarantelli, and V. Averbukh, *J. Chem. Phys.* **130**, 064104 (2009).
- ⁵²P. Kolorenč, V. Averbukh, K. Gokhberg, and L. S. Cederbaum, *J. Chem. Phys.* **129**, 244102 (2008).
- ⁵³M. Stener, P. Decleva, and A. Lisini, *Journal of Electron Spectroscopy and Related Phenomena* **74**, 29 (1995).
- ⁵⁴B. Schimmelpfennig, B. Nestmann, and S. Peyerimhoff, *J. Electron. Spectrosc. Relat. Phenom.* **74**, 173 (1995).
- ⁵⁵G. Grell, O. Kühn, and S. I. Bokarev, *Phys. Rev. A* **100**, 042512 (2019).
- ⁵⁶F. Holzmeier, T. J. A. Wolf, C. Gienger, I. Wagner, J. Bozek, S. Nandi, C. Nicolas, I. Fischer, M. Gühr, and R. F. Fink, *J. Chem. Phys.* **149**, 034308 (2018).
- ⁵⁷A. Kivimäki, M. Neeb, B. Kempgens, H. M. Köppe, and A. M. Bradshaw, *J. Phys. B At. Mol. Opt. Phys.* **29**, 2701 (1996).
- ⁵⁸C. D. Caldwell, S. J. Schaphorst, M. O. Krause, and J. Jiménez-Mier, *J. Electron Spectrosc. Relat. Phenom.* **67**, 243 (1994).
- ⁵⁹V. G. Wentzel, *Z. Physik* **43**, 524 (1927).
- ⁶⁰B. H. Bransden and C. J. Joachain, *Physics of Atoms and Molecules*, 1st ed. (Longman Scientific & Technical, Essex, 1983).
- ⁶¹F. W. J. Olver, D. W. Lozier, R. F. Boisvert, and C. W. Clark, eds., *NIST Handbook of Mathematical Functions*, 1st ed. (Cambridge University Press, 2010).
- ⁶²P.-O. Widmark, P. Å. Malmqvist, and B. O. Roos, *Theor. Chim. Acta* **77**, 291 (1990).
- ⁶³K. Kaufmann, W. Baumeister, and M. Jungen, *J. Phys. B At. Mol. Opt. Phys.* **22**, 2223 (1989).
- ⁶⁴J. Almlöf and P. R. Taylor, *J. Chem. Phys.* **86**, 4070 (1987).
- ⁶⁵I. Fernández Galván, M. Vacher, A. Alavi, C. Angeli, F. Aquilante, J. Autschbach, J. J. Bao, S. I. Bokarev, N. A. Bogdanov, R. K. Carlson, L. F. Chibotaru, J. Creutzberg, N. Dattani, M. G. Delcey, S. S. Dong, A. Dreuw, L. Freitag, L. M. Frutos, L. Gagliardi, F. Gendron, A. Giussani, L. González, G. Grell, M. Guo, C. E. Hoyer, M. Johansson, S. Keller, S. Knecht, G. Kovačević, E. Källman, G. Li Manni, M. Lundberg, Y. Ma, S. Mai, J. P. Malhado, P. Å. Malmqvist,

- P. Marquetand, S. A. Mewes, J. Norell, M. Olivucci, M. Oppel, Q. M. Phung, K. Pierloot, F. Plasser, M. Reiher, A. M. Sand, I. Schapiro, P. Sharma, C. J. Stein, L. K. Sørensen, D. G. Truhlar, M. Ugandi, L. Ungur, A. Valentini, S. Vancoillie, V. Veryazov, O. Weser, T. A. Wesolowski, P.-O. Widmark, S. Wouters, A. Zech, J. P. Zobel, and R. Lindh, *J. Chem. Theory Comput.* **15**, 5925 (2019).
- ⁶⁶M. J. Frisch, G. W. Trucks, H. B. Schlegel, G. E. Scuseria, M. A. Robb, J. R. Cheeseman, G. Scalmani, V. Barone, B. Mennucci, G. A. Petersson, H. Nakatsuji, M. Caricato, X. Li, H. P. Hratchian, A. F. Izmaylov, J. Bloino, G. Zheng, J. L. Sonnenberg, M. Hada, M. Ehara, K. Toyota, R. Fukuda, J. Hasegawa, M. Ishida, T. Nakajima, Y. Honda, O. Kitao, H. Nakai, T. Vreven, J. J. A. Montgomery, J. E. Peralta, F. Ogliaro, M. Bearpark, J. J. Heyd, E. Brothers, K. N. Kudin, V. N. Staroverov, R. Kobayashi, J. Normand, K. Raghavachari, A. Rendell, J. C. Burant, S. S. Iyengar, J. Tomasi, M. Cossi, N. Rega, J. M. Millam, M. Klene, J. E. Knox, J. B. Cross, V. Bakken, C. Adamo, J. Jaramillo, R. Gomperts, R. E. Stratmann, O. Yazyev, A. J. Austin, R. Cammi, C. Pomelli, J. W. Ochterski, R. L. Martin, K. Morokuma, V. G. Zakrzewski, G. A. Voth, P. Salvador, J. J. Dannenberg, S. Dapprich, A. D. Daniels, O. Farkas, J. B. Foresman, J. V. Ortiz, J. Cioslowski, and D. J. Fox, "Gaussian 09, Revision D.01," Tech. Rep. (Gaussian Inc., Wallingford, CT, 2009).
- ⁶⁷K. P. Huber and G. Herzberg, in *Molecular Spectra and Molecular Structure* (Springer, Boston, MA, 1979) pp. 8–689.
- ⁶⁸P.-Å. Malmqvist, A. Rendell, and B. O. Roos, *J. Phys. Chem.* **94**, 5477 (1990).
- ⁶⁹P. Å. Malmqvist, K. Pierloot, A. R. M. Shahi, C. J. Cramer, and L. Gagliardi, *J. Chem. Phys.* **128**, 204109 (2008).
- ⁷⁰B. O. Roos, P. R. Taylor, and P. Siegbahn, *Chem. Phys.* **48**, 157 (1980).
- ⁷¹K. Andersson, P. A. Malmqvist, B. O. Roos, A. J. Sadlej, and K. Wolinski, *J. Phys. Chem.* **94**, 5483 (1990).
- ⁷²F. Aquilante, J. Autschbach, R. K. Carlson, L. F. Chibotaru, M. G. Delcey, L. De Vico, I. F. Galván, N. Ferré, L. M. Frutos, L. Gagliardi, M. Garavelli, A. Giussani, C. E. Hoyer, G. Li Manni, H. Lischka, D. Ma, P. Å. Malmqvist, T. Müller, A. Nenov, M. Olivucci, T. B. Pedersen, D. Peng, F. Plasser, B. Pritchard, M. Reiher, I. Rivalta, I. Schapiro, J. Segarra-Martí, M. Stenrup, D. G. Truhlar, L. Ungur, A. Valentini, S. Vancoillie, V. Veryazov, V. P. Vysotskiy, O. Weingart, F. Zapata, and R. Lindh, *J. Comput. Chem.* **37**, 506 (2016).
- ⁷³P. Å. Malmqvist, *Int. J. Quantum Chem.* **30**, 479 (1986).
- ⁷⁴G. Bieri and L. Åsbrink, *J. Electron Spectrosc. Relat. Phenom.* **20**, 149 (1979).
- ⁷⁵O. Edqvist, E. Lindholm, L. E. Selin, and L. Åsbrink, *Phys. Scr.* **1**, 25 (1970).
- ⁷⁶S. Katsumata, H. Shiromaru, K. Mitani, S. Iwata, and K. Kimura, *Chemical Physics* **69**, 423 (1982).
- ⁷⁷P. Bolognesi, P. O’Keeffe, Y. Ovcharenko, L. Avaldi, and V. Carravetta, *J. Chem. Phys.* **136**, 154308 (2012).
- ⁷⁸K. Ueda, M. Okunishi, H. Chiba, Y. Shimizu, K. Ohmori, K. Sato, E. Shigemasa, and N. Kosugi, *Chem. Phys. Lett.* **236**, 311 (1995).
- ⁷⁹J. Schirmer, A. B. Trofimov, K. J. Randall, J. Feldhaus, A. M. Bradshaw, Y. Ma, C. T. Chen, and F. Sette, *Phys. Rev. A* **47**, 1136 (1993).
- ⁸⁰M. Higashi, E. Hiroike, and T. Nakajima, *Chem. Phys.* **68**, 377 (1982).
- ⁸¹O. M. Kvalheim, *Chem. Phys. Lett.* **86**, 159 (1982).
- ⁸²J. Feldhaus, W. Erlebach, A. L. D. Kilcoyne, K. J. Randall, and M. Schmidbauer, *Rev. Sci. Instrum.* **63**, 1454 (1992).
- ⁸³M. Banna and D. Shirley, *Chem. Phys. Lett.* **33**, 441 (1975).
- ⁸⁴C. Backx and M. J. V. der Wiel, *J. Phys. B: At. Mol. Phys.* **8**, 3020 (1975).
- ⁸⁵Y. Ma, C. T. Chen, G. Meigs, K. Randall, and F. Sette, *Phys. Rev. A* **44**, 1848 (1991).
- ⁸⁶S. L. Sorensen, R. Fink, R. Feifel, M. N. Piancastelli, M. Bässler, C. Miron, H. Wang, I. Hjelte, O. Björneholm, and S. Svensson, *Phys. Rev. A* **64**, 012719 (2001).
- ⁸⁷M. Neeb, J.-E. Rubensson, M. Biermann, W. Eberhardt, K. Randall, J. Feldhaus, A. Kilcoyne, A. Bradshaw, Z. Xu, P. Johnson, and Y. Ma, *Chemical Physics Letters* **212**, 205 (1993).
- ⁸⁸T. X. Carroll and T. D. Thomas, *J. Chem. Phys.* **89**, 5983 (1988).
- ⁸⁹M. Coreno, M. de Simone, K. C. Prince, R. Richter, M. Vondráček, L. Avaldi, and R. Camilloni, *Chem. Phys. Lett.* **306**, 269 (1999).
- ⁹⁰P. Kuiper and B. I. Dunlap, *The Journal of Chemical Physics* **100**, 4087 (1994).
- ⁹¹S. Schaphorst, C. Caldwell, M. Krause, and J. Jiménez-Mier, *Chemical Physics Letters* **213**, 315 (1993).
- ⁹²W. Wurth, J. Stöhr, P. Feulner, X. Pan, K. R. Bauchspiess, Y. Baba, E. Hudel, G. Rocker, and D. Menzel, *Phys. Rev. Lett.* **65**, 2426 (1990).
- ⁹³D. Lapiano-Smith, K. Lee, C.-I. Ma, K. T. Wu, and D. M. Hanson, *The Journal of Chemical Physics* **93**, 2169 (1990).
- ⁹⁴T. Gejo, Y. Takata, T. Hatsui, M. Nagasono, H. Oji, N. Kosugi, and E. Shigemasa, *Chemical Physics* **289**, 15 (2003).
- ⁹⁵M. Piancastelli, V. Carravetta, I. Hjelte, A. De Fanis, K. Okada, N. Saito, M. Kitajima, H. Tanaka, and K. Ueda, *Chem. Phys. Lett.* **399**, 426 (2004).
- ⁹⁶A. Jürgensen and R. G. Cavell, *Chemical Physics* **257**, 123 (2000).
- ⁹⁷J. Schirmer, L. Cederbaum, and W. Von Niessen, *Chemical Physics* **56**, 285 (1981).
- ⁹⁸G. Vall-Iloera, B. Gao, A. Kivimäki, M. Coreno, J. Álvarez Ruiz, M. de Simone, H. Ågren, and E. Rachlew, *The Journal of Chemical Physics* **128**, 044316 (2008).
- ⁹⁹D. Holland, A. Potts, L. Karlsson, M. Stener, and P. Decleva, *Chemical Physics* **390**, 25 (2011).
- ¹⁰⁰P. O’Keeffe, P. Bolognesi, A. R. Casavola, D. Catone, N. Zema, S. Turchini, and L. Avaldi, *Molecular Physics* **107**, 2025 (2009).
- ¹⁰¹A. W. Potts, D. M. P. Holland, A. B. Trofimov, J. Schirmer, L. Karlsson, and K. Siegbahn, *J. Phys. B: At. Mol. Opt. Phys.* **36**, 3129 (2003).
- ¹⁰²U. Lottermoser, P. Rademacher, M. Mazik, and K. Kowski, *Eur. J. Org. Chem.* **2005**, 522 (2005).
- ¹⁰³L. Storch, F. Tarantelli, S. Veronesi, P. Bolognesi, E. Fainelli, and L. Avaldi, *The Journal of Chemical Physics* **129**, 154309 (2008).
- ¹⁰⁴P. Bolognesi, P. O’Keeffe, Y. Ovcharenko, M. Coreno, L. Avaldi, V. Feyer, O. Plekan, K. C. Prince, W. Zhang, and V. Carravetta, *The Journal of Chemical Physics* **133**, 034302 (2010).